
TopoFisher: Learning Topological Summary Statistics by Maximizing Fisher Information

Matteo Biagetti^{1*} Mathieu Carrière² Francesco Conti²
 Enrico Maria Ferrari¹ Sven C. Heydenreich¹ Karthik Viswanathan³

¹Area Science Park, Padriciano 99, Trieste, Italy

²DataShape, Centre Inria d'Université Côte d'Azur, Sophia-Antipolis, France

³Institute of Physics, University of Amsterdam, Amsterdam

Abstract

Persistence diagrams provide stable, interpretable summaries of geometric and topological structure, and are useful for simulation-based inference when important information is not captured by low-order statistics. In practice, however, persistence-based pipelines require hand-chosen filtrations, vectorizations, and compressors, usually without an objective tied directly to parameter uncertainty. We introduce **TopoFisher**, a differentiable persistent-homology pipeline that learns topological summaries by maximizing local Gaussian Fisher information. From simulations near a fiducial parameter value, TopoFisher optimizes trainable filtrations, diagram vectorizations, and compressors without posterior samples or supervised regression targets, while preserving the inductive bias of stable topological descriptors. We also give sufficient regularity conditions under which the log-determinant Fisher loss is locally Lipschitz in the trainable parameters. Controlled experiments on noisy spirals and Gaussian random fields, where the total Fisher information is known, validate the pipeline: TopoFisher recovers a large fraction of the available information and improves over fixed topological vectorizations. Our main results are on weak gravitational lensing, a high-dimensional non-Gaussian field-inference problem from cosmology. There, both learned topological summaries, a fixed cubical filtration with a learned PersLay vectorization, and a learned CNN filtration with the same PersLay vectorization, reach $\log |F| \approx 21$, compared with 13.8 for the power spectrum, 17.1 for peak counts, and 19.3 for wavelet scattering, approaching an unconstrained Information Maximising Neural Network baseline (22.4) with up to $\sim 80\times$ fewer parameters. More importantly, the fixed-filtration variant generalizes better: under simulator shift from lognormal to LPT-based maps it retains $\log |F| = 19.24$ while the neural baseline drops to 8.9, and in neural posterior estimation it yields tighter constraints than the neural baseline, power spectrum, peak counts, and wavelet scattering. These results suggest Fisher-based topological optimizations as a robust, parameter-efficient front end for simulation-based inference.

*Corresponding author: matteo.biagetti@areasciencepark.it

1 Introduction

Parameter inference from high-dimensional data often relies on *summary statistics*: low-dimensional functions of observations that retain information about parameters of interest. This choice is especially important in simulation-based inference, where the likelihood $\log p(X|\theta)$ is intractable but samples can be generated from a simulator. Under standard regularity assumptions, the information carried by a summary statistic is quantified by its Fisher information matrix $F(\theta)$. By the Cramér–Rao bound, F^{-1} lower bounds the covariance of unbiased estimators, and maximizing $\log |F|$ minimizes the volume of the corresponding uncertainty ellipsoid [Tegmark, 1997]. Designing Fisher-informative summaries is therefore central to likelihood-free inference, from high-dimensional statistics [Giraud, 2014] to cosmology, where numerical simulations are routinely used to forecast and calibrate parameter constraints.

Topological Data Analysis (TDA) provides a useful class of such summaries through *persistence diagrams* (PDs). Built from persistent homology, PDs encode multiscale geometrical and topological features of data, such as connected components, loops, voids, and higher-dimensional cycles [Edelsbrunner et al., 2002, Carlsson, 2009]. In particular, their stability under perturbations of the input [Cohen-Steiner et al., 2007] makes them well-suited for inference, as well as their interpretability, as they often pinpoint meaningful structures in the data. In cosmology, for example, PD-based summaries have been shown to capture non-Gaussian information in galaxy and weak-lensing fields that is missed by classical two-point statistics Biagetti et al. [2021], Heydenreich et al. [2021].

However, practical PD-based pipelines require several manual choices. One must choose a filtration, which determines the ordering through which topological features are born and die; a vectorization, which maps diagrams to Euclidean features; and often a compressor, which reduces the final statistic to the parameter dimension. These choices strongly affect downstream inference, but are usually selected by hand rather than by a criterion tied to parameter uncertainty. Recent work on differentiable persistent homology shows that PDs and their vectorizations are almost everywhere differentiable with respect to filtration values [Carrière et al., 2021, Leygonie et al., 2022a], making gradient-based tuning possible. What remains unclear is the appropriate unsupervised objective for inference. This motivates our central question: **How can we automatically tune topological summaries so that they maximize Fisher information about the parameters of interest?**

Contributions. We introduce *TopoFisher*, a framework for learning topological summary statistics for simulation-based inference. Our contributions are:

- (i) We formulate persistence-based summary learning as Fisher-information maximization. The resulting pipeline can train filtrations, vectorizations, and compressors from simulations near a fiducial parameter value, without posterior samples or supervised regression targets.
- (ii) We provide a local well-posedness result for the Gaussian-Fisher loss of the learned summary: under boundedness, Lipschitz, and non-degeneracy assumptions, the negative log-determinant Gaussian-Fisher loss is locally Lipschitz in the trainable summary parameters.
- (iii) We validate the method on controlled benchmarks with known total Fisher information. On noisy spirals and Gaussian random fields, TopoFisher recovers a large fraction of the available information and consistently improves over fixed topological vectorizations.
- (iv) We show that TopoFisher is especially effective for weak gravitational lensing: it outperforms standard cosmological summaries, approaches the in-distribution Fisher information of an end-to-end Fisher-optimized IMNN, and is far more robust under simulator shift and posterior-level evaluation.

Related work. TopoFisher connects Fisher-based summary learning with differentiable topological data analysis. In simulation-based inference, high-dimensional data are often compressed before posterior estimation [Cranmer et al., 2020]. Classical optimal-compression methods preserve Fisher information locally through linear projections or score-based summaries [Heavens et al., 2000, Alsing and Wandelt, 2018, Alsing et al., 2018], while Information Maximising Neural Networks (IMNNs) train neural summaries near a fiducial parameter value by maximizing Fisher information [Charnock et al., 2018]. TopoFisher uses the same local Fisher principle, but constrains the learned summary to factor through persistent homology, yielding a structured and interpretable alternative to

black-box IMNN-style compression. In the experiments below, we therefore use an unconstrained IMNN as the main non-topological Fisher-neural reference.

Persistent homology provides stable multiscale topological descriptors [Edelsbrunner et al., 2002, Carlsson, 2009, Cohen-Steiner et al., 2007]. Many vectorizations have been proposed to map PDs to Euclidean space [Bubenik et al., 2015, Adams et al., 2017, Kusano et al., 2016, Carrière et al., 2017, Le and Yamada, 2018, Carrière et al., 2020], and recent work on differentiable persistence and learnable filtrations enables gradient-based optimization [Hofer et al., 2017, Gabrielsson et al., 2020, Hofer et al., 2020, Carrière et al., 2021, Leygonie et al., 2022b, Hacquard et al., 2022], mostly in supervised or regularization-driven settings. TopoFisher instead trains topological summaries by the Fisher information they retain.

Persistent homology has also been applied in physics, biology, medicine, materials science, and related fields (see Hensel et al. [2021] for a review). In cosmology, PD-based summaries have been used for cosmic-web analysis, random-field morphology, and weak-lensing inference [Pranav et al., 2017, 2019, Biagetti et al., 2021, Heydenreich et al., 2021, 2022, Yip et al., 2024]. These works typically fix the filtration and vectorization by hand; TopoFisher learns them from simulations using the same Fisher criterion used to evaluate parameter constraints.

2 The TopoFisher Loss

TopoFisher is a trainable summary map: data are filtered, converted into persistence diagrams, vectorized into Euclidean features, and compressed to a low-dimensional statistic. Instead of choosing these stages by hand, we optimize their trainable parameters by maximizing the Fisher information of the summary at a fiducial parameter value. This section introduces the required ingredients and then defines the TopoFisher loss.

Persistent homology in brief. A key component of TopoFisher are *persistence diagrams* (PDs), which are built from the theory of *persistent homology* (PH); see Appendix A and Edelsbrunner and Harer [2010a], Oudot [2015] for more details.

Given a topological space T , the starting point of PH is to define a *filtration*, i.e., a finite sequence of growing subspaces $T_1 \subseteq \dots \subseteq T_N \subseteq T$. The filtration depends on the data: for a point cloud, one can grow balls of increasing radius around the points (*Vietoris–Rips filtration*); for a grayscale image $f : P \rightarrow \mathbb{R}$ on a pixel grid, one can use sublevel sets $T_i = f^{-1}((-\infty, \alpha_i])$ for increasing thresholds (*cubical filtration*)².

PH then tracks the *topological features* (connected components, loops, cavities) that appear and disappear along the filtration, recording for each a birth time b_i and death time d_i . A *persistence diagram* summarizes this as a set of points $(b_i, d_i) \in \mathbb{R}^2$, with $\|d_i - b_i\|$ the *persistence* of the feature.

PDs enjoy two properties central to TopoFisher. They are *stable* Cohen-Steiner et al. [2007]: close filtrations yield close diagrams under appropriate metrics. And when a filtration is smoothly parametrized by trainable parameters ϕ , the resulting diagram $\text{Dgm}_k(f_\phi)$ is piecewise differentiable in ϕ Carrière et al. [2021], Leygonie et al. [2022a], enabling gradient-based optimization. Since the space of PDs is not Euclidean, downstream pipelines apply a *vectorization* (e.g. persistence landscapes Bubenik et al. [2015], persistence images Adams et al. [2017], or learnable layers such as PersLay Carrière et al. [2020]) before further processing.

Fisher Information and Summary Statistics. For a parametric system with data X , a random variable taking values in a measurable space \mathcal{X} , let $\{p(\cdot|\theta)\}_{\theta \in \Theta}$ be a family of probability densities on \mathcal{X} , with $\Theta \subseteq \mathbb{R}^d$ open. The Fisher Information (FI) (Fisher [1925], Kendall and Stuart [1979]) at a fiducial parameter θ_{fid} is defined as:

$$F_X(\theta) = \mathbb{E}_\theta \left[\nabla_\theta \log p(X|\theta) \nabla_\theta \log p(X|\theta)^\top \right]. \quad (1)$$

We call $F_X(\theta)$ the total Fisher information, since it quantifies the information available in the uncompressed observation X : via the Cramér–Rao bound, under standard regularity conditions

²Two standard realizations exist: the V-construction on vertices (lower-star filtration) and the T-construction on top-dimensional cubes; both are used in this work (Appendix J.2).

[Lehmann and Casella, 1998], $(nF_X(\theta))^{-1}$ sets the matrix lower limit on the covariance of any unbiased estimator of θ based on n i.i.d. samples. Accordingly, the log-determinant $\log |F_X|$ provides a scalar measure of this total information.

In this work, we focus on complex physical systems where the likelihood $p(X|\theta)$ is often analytically intractable. This restricts our framework to a simulation-based regime, where we only assume the capacity to sample realizations $X \sim p(\cdot|\theta)$. In such cases, the high dimensionality of the data-space \mathcal{X} renders direct inference or comparison prohibitive due to the curse of dimensionality [Alsing et al., 2018]. To circumvent this, we compress the data via a parametric summary mapping of the following form: $s_\phi: \mathcal{X} \rightarrow \mathbb{R}^M$ given by

$$s_\phi := C_\phi \circ V_\phi \circ \text{Dgm}_k \circ f_\phi, \quad (2)$$

where f_ϕ is a learnable filtration, Dgm_k^3 is the persistence diagram operator in dimension k , V_ϕ is a vectorization, and C_ϕ is a compressor to \mathbb{R}^M . The parameters $\phi \in \Phi \subseteq \mathbb{R}^p$ are learned and the target dimension $M \ll n$ is typically of the same order than the degrees of freedom of the system.

This mapping induces a distribution $q_\phi(\cdot|\theta)$ on the summary space. The FI of the transformed system, $F_\phi(\theta)$, is defined analogously to Eq. (1) but w.r.t. the distribution q_ϕ . Crucially, the Data Processing Inequality [Cover and Thomas, 2006] implies that $\log |F_\phi(\theta_{\text{fid}})| \leq \log |F_X(\theta_{\text{fid}})|$, meaning that the log-determinant of the total FI represents a global information ceiling. Our goal is thus to optimize ϕ to close this gap, so that s_ϕ preserves the maximum information relevant for inferring θ .

Assumptions and Fisher estimation. To estimate the Fisher information of the learned summary, we use the standard local Gaussian approximation

$$q_\phi(\cdot|\theta) \simeq \mathcal{N}(\mu_\phi(\theta), \Sigma_\phi)$$

near the fiducial parameter θ_{fid} , with covariance treated as locally independent of θ . Under this approximation, the Gaussian Fisher information reduces to

$$F_\phi^G(\theta_{\text{fid}}) = J_\theta \mu_\phi(\theta_{\text{fid}})^\top \Sigma_\phi^{-1} J_\theta \mu_\phi(\theta_{\text{fid}}), \quad (3)$$

where J_θ indicates the Jacobian with respect to parameters θ . In practice, we estimate Eq. (3) from a structured batch \mathcal{B} of simulation data. Thus, in what follows, F_ϕ^G denotes the population Gaussian-Fisher matrix of the summary, while $\widehat{F}_{\phi, \mathcal{B}}^G$ denotes its finite-sample estimate. More details on the Fisher estimation are provided in Appendix B.

Loss and gradients. To maximize the information content of our topological summaries, we define the TopoFisher loss as:

$$\widehat{\mathcal{L}}_{\mathcal{B}}(\phi) = -\log \left| \widehat{F}_{\phi, \mathcal{B}}^G(\theta_{\text{fid}}) \right|, \quad (4)$$

which we minimize via stochastic subgradient descent with respect to ϕ . This objective is computed using the Fisher matrix estimated from the batch \mathcal{B} , $\widehat{F}_{\phi, \mathcal{B}}^G$. Although persistent homology is not differentiable everywhere, we leverage the subdifferentiable framework established by Leygonie et al. [2022b] and Carrière et al. [2021], which ensures well-defined gradients for optimization.

3 Stability

We identify minimal regularity conditions under which the log-determinant of the Gaussian Fisher information of Eq. (3) is locally Lipschitz in ϕ . The result applies to any pipeline whose summary s_ϕ satisfies the assumptions below, not only persistence-based ones, and is distinct from the classical regularity of $\theta \mapsto F_X^G(\theta)$ in the physical parameters [Vaart, 1998]. To our knowledge, no such analysis has been made explicit for Fisher-optimized differentiable persistence pipelines.

Assumption 3.1. *The summary map s_ϕ , the covariance Σ_ϕ , the Jacobian $J_\theta \mu_\phi(\theta_{\text{fid}})$, and the Fisher information matrix $F_\phi^G(\theta_{\text{fid}})$ satisfy the following:*

- (i) $\|s_{\phi'}(X) - s_\phi(X)\| \leq L_s \|\phi' - \phi\|$ for all $\phi, \phi' \in \Phi$ and every realization X ;

³We present the following for a single homological dimension k ; the case of using multiple dimensions follows immediately, concatenating the resulting vectors prior to the compression.

- (ii) $\sup_{\phi \in \Phi} \mathbb{E}[\|s_\phi(X)\|^2] \leq M^2$;
- (iii) $\|\Sigma_\phi^{-1}\|_{\text{op}} \leq \kappa_\Sigma$ for all $\phi \in \Phi$;
- (iv) $\|J_\theta \mu_{\phi'}(\theta_{\text{fid}}) - J_\theta \mu_\phi(\theta_{\text{fid}})\|_{\text{op}} \leq L_J \|\phi' - \phi\|$ for all $\phi, \phi' \in \Phi$;
- (v) $\lambda_{\min}(F_\phi(\theta_{\text{fid}})) > 0$ for all $\phi \in \Phi$,

where $\lambda_{\min}(A)$ denotes the smallest eigenvalue of A . Under these assumptions, we obtain the following stability result, whose proof can be found in Appendix C.

Theorem 3.2. *Let $F_\phi^G(\theta_{\text{fid}})$ be the Fisher information matrix as in Eq. (3), and let $\mathcal{L}: \Phi \rightarrow \mathbb{R}$ be defined as $\mathcal{L}(\phi) = -\log |F_\phi^G(\theta_{\text{fid}})|$. Then, under Assumptions 3.1(i)–(v), \mathcal{L} is locally Lipschitz on Φ . More precisely, for every $\phi \in \Phi$ there exist $\varepsilon_0(\phi) > 0$ and $K(\phi) > 0$, depending on κ_Σ , L_s , M , L_J , $\|J_\theta \mu_\phi(\theta_{\text{fid}})\|_{\text{op}}$, and $\lambda_{\min}(F_\phi^G(\theta_{\text{fid}}))$, such that for all $\phi' \in \Phi$ with $\|\phi' - \phi\| < \varepsilon_0(\phi)$,*

$$|\mathcal{L}(\phi') - \mathcal{L}(\phi)| \leq K(\phi) \|\phi' - \phi\|. \quad (5)$$

Proof idea. The proof proceeds in three steps. First, Assumptions 3.1 (i) – (iii) yield local Lipschitz continuity of $\phi \mapsto \Sigma_\phi^{-1}$ via the resolvent identity $A^{-1} - B^{-1} = A^{-1}(B - A)B^{-1}$. Combined with the Lipschitz Jacobian assumption (iv), this propagates to $\phi \mapsto F_\phi^G(\theta_{\text{fid}})$. Finally, non-degeneracy (v) and Weyl’s inequality keep $F_\phi^G(\theta_{\text{fid}})$ uniformly positive definite along short segments, so that a standard log-determinant perturbation bound transfers the Lipschitz property to \mathcal{L} .

Well-posedness of gradient-based training. Theorem 3.2 concerns the loss \mathcal{L} ; at training time we optimize the sample-based estimator $\widehat{\mathcal{L}}_{\mathcal{B}}$, which differs from \mathcal{L} by finite-sample noise on $\widehat{\Sigma}_\phi$ and on the perturbed-point means, and by the truncation bias of the central-difference Jacobian. We do not formally transfer the regularity result to $\widehat{\mathcal{L}}_{\mathcal{B}}$; the impact of these effects is monitored empirically through the diagnostics of Appendix B. Note however that, upon using batches of larger sizes and more computational power, our estimated loss $\widehat{\mathcal{L}}_{\mathcal{B}}$ will get closer to \mathcal{L} , ensuring that our theoretical guarantees hold in practice.

4 Experiments

We evaluate TopoFisher on three benchmarks: noisy spiral point clouds and 2D Gaussian random fields, where the total Fisher information is known, and weak gravitational lensing maps, a high-dimensional non-Gaussian inference problem with no closed-form optimal summary. Across experiments, we compare fixed TDA summaries, TopoFisher-optimized TDA summaries, and unconstrained neural baselines. Performance is measured by $\log |F|$ and, when available, by efficiency relative to the total Fisher information, $\eta_{\log} = \log |\widehat{F}^G| / \log |F_X|$. Training and evaluation details are given in Appendix J.

4.1 Noisy spiral point clouds

We consider 2D point clouds $X \in \mathbb{R}^{N \times 2}$ with $N = 240$ points, sampled independently from a mixture of a uniform background on $[-h, h]^2$ (with probability $\lambda = 40/240$) and a noisy spiral $(1 - \lambda)$. The spiral coordinates are defined by an angular variable $t \sim \mathcal{U}(0, 4\pi)$ and a radius $r \sim \mathcal{N}(\mu t, w^2)$. The target parameters are $\theta = (\mu, w)$, where μ controls the radial expansion and w the intrinsic width. For each fiducial configuration θ_{fid} , we generate $n_s = n_d = 10,000$ samples for covariance and derivative estimation for each 5 independent seeds. Since the mixture density $p(X|\theta)$ is known, the total Fisher matrix F_X admits an integral expression (see Appendix E for a derivation), which we use to compute the efficiency metric η_{\log} .

Methods. All methods share a common preprocessing step: for each point x in the cloud, they operate on the k -nearest neighbor distances $d_k(x) \in \mathbb{R}^k$ to ensure global isometryUe invariance. Given a point cloud X , we first construct an Alpha complex K to capture the connectivity of the points, and parametrize a scalar function f_ϕ on the vertices of the complex via two architectures:

- *TF-TDA-MLP*. The vertex values are defined as $f_\phi(x) = g_\phi(d_k(x))$, where g_ϕ is a Multi-Layer Perceptron processing each point locally.
- *TF-TDA-GNN*. Features $d_k(x)$ are propagated across the 1-skeleton of K using a Graph Neural Network to produce $f_\phi(x)$, better capturing relational structure.

To ensure a valid simplicial filtration, we extend f_ϕ to edges as $f_\phi(e_{ij}) = \|x_i - x_j\| + \max\{f_\phi(x_i), f_\phi(x_j)\}$, and to higher-dimensional simplices with a lower-star construction: $f_\phi(\sigma) = \max_{e \subset \sigma} f_\phi(e)$. The resulting persistence diagrams in homological dimensions 0 and 1 are converted into 8×8 differentiable persistence images, flattened, and compressed to \mathbb{R}^2 via a small MLP.

We compare these against: (i) *DTM*, a non-learnable TDA reference where f_ϕ is replaced by the fixed distance-to-measure function $g(d_k(x)) = ((1/k) \sum_j d_{k,j}(x)^2)^{1/2}$, while keeping the rest of the pipeline identical; (ii) *MLP-only* and *GNN-only*, which serve as neural references. These models use the same architectures described above to learn a 2D function of the point clouds, but aggregate the local contributions of each point via sum-pooling, thereby bypassing the persistence computation.

Results. Table 1 reports results at $\theta_{\text{fid}} = (\mu_{\text{fid}}, w_{\text{fid}}) = (0.6, 0.1)$ for $k = 100$. The TF-TDA-MLP pipeline recovers 78.2% of the total log-determinant Fisher score, exceeding the fixed-filtration DTM baseline by 8.1% and matching the unconstrained MLP-only model (78.1%) within cross-seed variance. TF-TDA-GNN underperforms DTM, while GNN-only remains competitive but below MLP-only: at $k = 100$ the local context of each point already contains enough information about the spiral geometry, and the additional relational complexity of message passing appears redundant for this inference task. Results at four additional fiducial configurations are reported in Appendix F and reproduce the same ranking.

Beyond the quantitative match with the unconstrained model, the learned filtration is *interpretable*: visualizations show that the MLP assigns vertex values that progressively “unroll” the spiral, effectively filtering out background noise and highlighting the manifold backbone, while the black box models do not show any visible structure in the learned function (see Figures 1 and 2 in Appendix F).

Table 1: Spiral results at $\theta_{\text{fid}} = (0.6, 0.1)$ and $k = 100$, averaged over 5 seeds. Constraint column reports $(\sigma(\mu), \sigma(w))$. We prefix TopoFisher-trained summaries with *TF-*; DTM is a fixed-topology ablation, and MLP/GNN-only are unconstrained non-topological references.

Method	$\log F $	(σ_μ, σ_w)	η_{\log}
<i>Total</i>	24.27	(0.005, 0.001)	100%
<i>Fixed topological ablation: persistence without TopoFisher learning</i>			
DTM fixed filtration	17.18 ± 0.06	(0.014, 0.013)	70.1%
<i>TopoFisher summaries: our learned topological contributions</i>			
TF-TDA-MLP	18.99 ± 0.30	(0.013, 0.006)	78.2%
TF-TDA-GNN	16.20 ± 0.19	(0.016, 0.019)	66.7%
<i>Unconstrained neural references: non-topological summaries</i>			
MLP-only	18.96 ± 0.58	(0.012, 0.006)	78.1%
GNN-only	18.26 ± 0.25	(0.015, 0.007)	75.2%

4.2 Gaussian random fields

We use two-dimensional Gaussian random fields (GRFs) as a controlled benchmark because their likelihood is known and the Fisher information in the full field can be computed analytically. Each sample is a zero-mean periodic field on a 64×64 grid. In Fourier space, the modes are independent Gaussian random variables with variance given by the power spectrum $P(k) = A_s (k/k_{\text{pivot}})^{-B}$, where A_s controls the overall amplitude of the field, while B controls how power is distributed across spatial scales. We choose the pivot scale $k_{\text{pivot}} = \exp(\ln k)$, where the average is over the nonzero Fourier modes, so that the Fisher correlation between A_s and B vanishes at the fiducial point.

We consider fiducial parameters $\theta_{\text{fid}} = (A_s, B) = (1, B_0)$ with $B_0 \in \{-2, -1, 0, 1, 2\}$, use finite-difference steps $\Delta\theta = (0.1, 0.1)$, and generate $n_s = n_d = 40,000$ simulations per configuration over 5 independent seeds. The standard Gaussian-field Fisher formula, derived in Appendix G, gives the same total information for all values of B_0 : $\log |F_X| = 13.89$, corresponding to $\sigma(A_s) = 0.022$ and $\sigma(B) = 0.044$. This value provides an absolute information ceiling against which all learned and fixed summaries can be compared.

Methods. We compare fixed and learnable topological summaries, together with a non-topological CNN baseline. All TDA methods compute H_0 and H_1 cubical persistence on periodic fields. Fixed-filtration methods use the raw field as the cubical filtration, whereas learnable-filtration methods first transform the field with a small CNN and then compute cubical persistence on the CNN output. All resulting feature vectors are compressed to two dimensions with MOPED [Heavens et al., 2000], a locally linear Fisher-preserving Gaussian compression that is detailed in Appendix B.

Fixed topological baselines. As a topological baseline without TopoFisher optimization, we use a fixed cubical filtration with three hand-designed vectorizations: (i) persistence images [Adams et al., 2017] of size 8×8 with persistence weighting and bandwidth 1; (ii) uniformly weighted persistence silhouettes [Chazal et al., 2014] on 50 grid points; and (iii) differentiable persistence curves of birth and death values [Biagetti et al., 2021], also on 50 grid points. We refer to these as Cubical-PI, Cubical-Silhouette, and Cubical-Curves, respectively. Full definitions are given in Appendix J.3.

Learnable topological summaries. Cubical-PersLay keeps the cubical filtration fixed but learns the diagram vectorization with PersLay [Carrière et al., 2020], a permutation-invariant set network applied to persistence diagram points. We use a 16-dimensional point embedding followed by a 32-hidden-unit MLP for each homology class, with spectral normalization for Lipschitz control. TF-CNN-PersLay additionally prepends a two-layer CNN with 8 hidden channels and 3×3 kernels, yielding a learned filtration before the same PersLay vectorization and MOPED compression.

Non-topological Fisher-neural baseline. As a black-box reference, we use an IMNN [Charnock et al., 2018]: a strided convolutional encoder followed by a dense head that directly outputs two summaries, one per parameter. The persistence and vectorization stages are replaced by the identity, and no MOPED compression is applied; the dense head is the learned compressor. The IMNN is trained end-to-end with the same local Gaussian Fisher objective used by TopoFisher, making it a direct comparison between an unconstrained Fisher-optimized neural summary and a topologically structured Fisher-optimized summary. Architectural details are provided in Appendix J.2.

Total Fisher Information baseline. The total Fisher of a power-law GRF on a fixed $N \times N$ grid does not depend on B_0 (see a derivation in Appendix G): both diagonal entries of $F(\theta)$ are functions only of the lattice mode structure and of A_s . Each of the five B_0 values therefore provides an independent benchmark with the same theoretical ceiling $\log |F_X| = 13.89$, and the natural figure of merit for a method is its mean performance across this range.

Results. Table 2 reports the mean performance of each pipeline on the GRF benchmark. The best method is TF-Cubical-PersLay, which reaches 90.9% of the total log-determinant Fisher score and outperforms all fixed-vectorization topological baselines by a large margin. The learnable-filtration variant TF-CNN-PersLay also improves over the fixed-vectorization baselines, but does not surpass TF-Cubical-PersLay. We discuss this aspect in the next section.

The non-topological IMNN baseline reaches 88.4% of the total Fisher information, comparable to the learnable topological methods. The topological pipelines, however, achieve this performance with roughly $55 \times$ fewer trainable parameters: TF-Cubical-PersLay has 1,376 trainable parameters and TF-CNN-PersLay has 2,049, compared with approximately 7.5×10^4 for the GRF IMNN. This suggests that the persistence-based inductive bias provides a parameter-efficient route to high-Fisher summaries without sacrificing constraining power.

4.3 Weak gravitational lensing

Weak gravitational lensing measures the convergence field κ , the line-of-sight projection of matter density inferred from coherent distortions of background-galaxy shapes. Its statistics constrain cosmological parameters such as (Ω_m, σ_8) , which control the matter density and amplitude of structure. Because κ is highly non-Gaussian on the scales of interest, the angular power spectrum

Table 2: GRF results at $N = 64$, averaged over $B_0 \in \{-2, -1, 0, 1, 2\}$ and 5 seeds per B_0 . Constraint column reports $(\sigma(A_s), \sigma(B))$. The total Fisher information is $\log |F_X| = 13.89$ at every B_0 . We prefix TopoFisher-trained summaries with *TF-*.

Method	$\log F $	(σ_{A_s}, σ_B)	η_{\log}
<i>Total</i>	<i>13.89</i>	<i>(0.022, 0.044)</i>	<i>100%</i>
<i>Fixed topological ablations: persistence without TopoFisher learning</i>			
Cubical-PI	11.53 ± 0.56	(0.037, 0.093)	83.0%
Cubical-Silhouette	10.68 ± 0.55	(0.046, 0.129)	76.9%
Cubical-Curves	9.22 ± 1.28	(0.086, 0.292)	66.4%
<i>TopoFisher summaries: our learned topological contributions</i>			
TF-Cubical-PersLay	12.63 ± 0.37	(0.032, 0.061)	90.9%
TF-CNN-PersLay	12.07 ± 0.15	(0.034, 0.071)	87.7%
<i>Unconstrained Fisher-neural reference: non-topological summary</i>			
IMNN	12.29 ± 0.09	(0.032, 0.067)	88.4%

C_ℓ is suboptimal and no closed-form optimal summary is known [Kilbinger, 2015, Ribli et al., 2019, Cheng et al., 2020, Allys et al., 2020]. This makes weak lensing a natural testbed for learned summary statistics. We use the `sbi_lens` lognormal and Lagrange Perturbation Theory (LPT) simulators [List et al., 2023] to generate 512×512 convergence maps over a $10^\circ \times 10^\circ$ field of view and five tomographic redshift bins. For each of five independent seeds, we generate 20,000 maps at the fiducial cosmology and at each finite-difference point. All maps are Gaussian-smoothed with $\sigma = 2'$ before applying any summary statistic.

We report three evaluations in Table 3. Local Fisher measures Gaussian Fisher information on lognormal maps at the fiducial cosmology. Transfer Fisher trains learned feature extractors on lognormal maps, freezes them, and evaluates on LPT maps. For MOPED-based summaries we re-estimate the covariance, finite-difference Jacobian, precision matrix, and MOPED compressor on the LPT evaluation bank; for the IMNN the frozen two-dimensional network output is used directly and only the Fisher statistics are re-estimated. No IMNN, CNN-filtration, or PersLay weights are retrained on LPT. Finally, NPE posterior performance is measured by training a neural posterior estimator over a prior and reporting the posterior covariance of (Ω_m, σ_8) . In all Fisher evaluations, we use an additive auto-bin approximation across the five tomographic bins, rather than a full joint tomographic Fisher matrix with cross-bin covariances.

Methods. As the total Fisher is unknown, we compare against three cosmological baselines: (i) the angular power spectrum of the log-transformed field, $\log(C_\ell)$; (ii) peak counts, a histogram of local convergence maxima sensitive to halo-like over-densities; and (iii) the wavelet scattering transform (WST) [Villar-Corrales and Morgenshtern, 2021], a state-of-the-art non-Gaussian summary built from a cascade of wavelet convolutions and pointwise moduli. We use the same learnable topological pipelines as Section 4.2, adapted to 512^2 inputs, and the same IMNN reference (CNN encoder + dense two-dimensional summary head, trained end-to-end by the local Gaussian Fisher objective).

Results. Table 3 summarizes the local Fisher, transfer Fisher, and NPE posterior evaluations. In distribution, all topological summaries outperform the two-point baseline $\log(C_\ell)$, which reaches only $\log |F| = 13.8$ with marginal constraints $(\sigma_{\Omega_m}, \sigma_{\sigma_8}) = (0.039, 0.059)$. This confirms that persistent homology captures non-Gaussian information in the smoothed convergence field that is inaccessible to the power spectrum. Learning the diagram vectorization gives a further substantial gain: both TopoFisher variants, TF-Cubical-PersLay and TF-CNN-PersLay, reach $\log |F| \approx 21.5$ with marginal constraints near (0.008, 0.008), within ~ 0.9 nats of the unconstrained IMNN reference ($\log |F| = 22.4$) trained end-to-end with the identical Fisher objective. Crucially, this near-parity is achieved while retaining an explicitly topological representation and using up to $\sim 80\times$ fewer trainable parameters than the IMNN (see Appendix J.2 for parameter counts).

A consistent pattern across both lensing and the GRF benchmark is that learning the vectorization alone is at least as effective as jointly learning a CNN filtration and a PersLay vectorization, and is substantially more robust. On lensing, TF-Cubical-PersLay and TF-CNN-PersLay are statistically indistinguishable in local Fisher (21.51 ± 0.02 versus 21.48 ± 0.13). Under simulator shift, TF-Cubical-PersLay retains $\log |F| = 19.2$ while TF-CNN-PersLay collapses to 12.7, a degradation comparable to that of fixed-vectorization topological baselines such as Cubical-PI ($19.2 \rightarrow 10.8$). The same ranking persists at the posterior level: TF-Cubical-PersLay reaches $\log |F| = 16.7$ on NPE while TF-CNN-PersLay drops to 14.7. We attribute this pattern to the cubical sublevel filtration being already well matched to scalar cosmological fields: persistence pairs of the raw convergence map directly encode the prominence and nesting of peaks, voids, and surrounding structures. Adding a learnable CNN filtration enlarges the search space, but many directions mainly reparameterize filtration values or alter persistence pairings in non-smooth, simulator-specific ways, rather than increasing the information ceiling. For these fields, the most effective TopoFisher design is therefore modular: keep the physically meaningful cubical filtration fixed and learn how to aggregate its diagram points.

The transfer and NPE evaluations sharpen this picture. Under lognormal-to-LPT shift the IMNN drops from $\log |F| = 22.4$ to 8.9 with weak constraints (0.19, 0.30), while TF-Cubical-PersLay retains 19.2, the best transfer determinant by a wide margin. On NPE, despite its higher local Fisher, the IMNN yields the weakest posterior (14.3), whereas TF-Cubical-PersLay achieves the tightest constraints overall: $\log |F| = 16.7$ with $(\sigma_{\Omega_m}, \sigma_{\sigma_8}) = (0.03, 0.04)$. Taken together, these results indicate that Fisher optimization alone is not sufficient: the unconstrained IMNN, despite its higher in-distribution Fisher information, transfers poorly and yields the weakest posterior constraints, whereas the same Fisher objective combined with a topological inductive bias produces summaries that retain most of their information under simulator shift and dominate at the posterior level. The gain attributable to topology, separated from Fisher optimization itself, is the difference between TF-Cubical-PersLay and the IMNN along the transfer and NPE axes. Further details can be found in Appendix I.

Table 3: Weak lensing at $\sigma = 2'$ smoothing for (Ω_m, σ_8) , additive over 5 tomographic bins. Constraint columns report $(\sigma_{\Omega_m}, \sigma_{\sigma_8})$. Transfer freezes the lognormal-trained feature extractors and evaluates Fisher information on LPT maps. MOPED/Fisher statistics are re-estimated on the LPT evaluation bank when applicable; the IMNN uses its frozen 2-D output directly. Row groups separate external baselines, ablations, TopoFisher contributions, and the unconstrained Fisher-neural reference.

Method	Local Fisher		Transfer Fisher		NPE posterior	
	$\log F $	$(\sigma_{\Omega_m}, \sigma_{\sigma_8})$	$\log F $	$(\sigma_{\Omega_m}, \sigma_{\sigma_8})$	$\log F $	$(\sigma_{\Omega_m}, \sigma_{\sigma_8})$
<i>Cosmology baselines</i>						
$\log(\mathcal{C}_\ell)$	13.78 ± 0.08	(0.039, 0.059)	12.87 ± 0.05	(0.046, 0.086)	15.77 ± 0.05	(0.042, 0.052)
Peak counts	17.14 ± 0.01	(0.026, 0.020)	11.61 ± 0.07	(0.119, 0.165)	15.30 ± 0.20	(0.038, 0.055)
Wavelet scattering	19.27 ± 0.01	(0.013, 0.011)	12.55 ± 0.04	(0.044, 0.090)	16.50 ± 0.39	(0.034, 0.051)
<i>Fixed topological ablations: persistence without TopoFisher learning</i>						
Cubical-Silhouette	16.37 ± 0.02	(0.029, 0.031)	12.43 ± 0.01	(0.082, 0.128)	15.76 ± 0.42	(0.039, 0.054)
Cubical-Curves	18.08 ± 0.01	(0.019, 0.016)	1.98 ± 0.60	(1.340, 2.052)	12.83 ± 0.24	(0.071, 0.097)
Cubical-PI	19.17 ± 0.01	(0.014, 0.012)	10.84 ± 0.02	(0.175, 0.271)	15.11 ± 0.60	(0.041, 0.064)
<i>TopoFisher summaries: our learned topological contributions</i>						
TF-Cubical-PersLay	21.51 ± 0.02	(0.008, 0.009)	19.24 ± 0.02	(0.063, 0.095)	16.72 ± 0.51	(0.031, 0.044)
TF-CNN-PersLay	21.48 ± 0.13	(0.007, 0.005)	12.72 ± 0.16	(0.073, 0.110)	14.74 ± 0.59	(0.051, 0.060)
<i>Unconstrained Fisher-neural reference: black-box non-topological summary</i>						
IMNN	22.35 ± 0.05	(0.006, 0.004)	8.92 ± 0.90	(0.247, 0.391)	14.32 ± 0.33	(0.050, 0.077)

5 Conclusions

We introduced TopoFisher, a framework for learning persistence-based summary statistics by maximizing the local Gaussian Fisher information of the final summary, turning filtration, vectorization, and compression choices into trainable components while constraining the summary to factor through stable topological descriptors. We complemented this with a local well-posedness result: under mild

boundedness, Lipschitz, and non-degeneracy conditions, the negative log-determinant Gaussian-Fisher loss is locally Lipschitz in the trainable parameters.

The central empirical finding is that Fisher optimization and topology play complementary roles: the unconstrained IMNN achieves the highest in-distribution Fisher information but transfers poorly and yields the weakest posterior, whereas the same objective combined with a topological inductive bias produces summaries that generalize and dominate at the posterior level with 50 – 100× fewer parameters. The topological factorization is what makes Fisher-based summary learning robust enough for simulation-based inference.

TopoFisher is a *local* summary-design method: it optimizes Fisher information near a fiducial point under a Gaussian summary approximation, and provides no guarantee of globally injective summaries or calibrated posteriors over a wide prior volume. A natural extension includes learning summaries jointly across multiple fiducials to broaden the regime of validity.

Code availability

The code used to run the TopoFisher experiments, generate configurations, train the models, and reproduce the Fisher, transfer, and simulation-based inference evaluations is available at <https://github.com/RitAreaSciencePark/TopoFisher>. The repository includes instructions for regenerating the simulation datasets and reproducing the main tables and figures. Large generated simulation datasets are not included in the repository because of their size, but they can be regenerated from the documented scripts and configuration files.

Acknowledgements

M.B. and E.M.F. are supported by the Ministero Università e Ricerca, project E-ARGO” (CUP J95F21002190001), with title “Fondo finalizzato al rilancio degli Investimenti delle Amministrazioni Centrali dello Stato e allo sviluppo del Paese, ex Art.1, comma 14, legge n. 160/2019”. M.C. and F.C. are supported by l’Agence Nationale de la Recherche (ANR) under grants TopModel ANR-23-CE23-0014. MC is also supported by 3IA ANR-23-IACL-0001. S.C.H. is supported by the European Union – NextGenerationEU within the project PNRR “Finanziamento di progetti presentati da giovani ricercatori” - Mission 4 Component 2 investment 1.2.

We thank Area Science Park supercomputing platform ORFEO made available for conducting the research reported in this paper and the technical support of the Laboratory of Data Engineering staff.

References

- Max Tegmark. Measuring Cosmological Parameters with Galaxy Surveys. *Phys. Rev. Lett.*, 79(20): 3806–3809, November 1997. doi: 10.1103/PhysRevLett.79.3806.
- Christophe Giraud. *Introduction to High-Dimensional Statistics*. Chapman and Hall/CRC, 1 edition, 2014. doi: 10.1201/b17895. URL <https://doi.org/10.1201/b17895>.
- Herbert Edelsbrunner, David Letscher, and Afra Zomorodian. Topological persistence and simplification. *Discrete & Computational Geometry*, 28:511–533, 2002.
- Gunnar Carlsson. Topology and data. *Bulletin of the American Mathematical Society*, 46(2):255–308, 2009.
- David Cohen-Steiner, Herbert Edelsbrunner, and John Harer. Stability of persistence diagrams. *Discrete & Computational Geometry*, 37(1):103–120, 2007.
- Matteo Biagetti, Alex Cole, and Gary Shiu. The persistence of large scale structures. Part I: Primordial non-Gaussianity. *Journal of Cosmology and Astroparticle Physics*, 2021(04):061, 2021.
- Sven Heydenreich, Benjamin Brück, and Joachim Harnois-Déraps. Persistent homology in cosmic shear: Constraining parameters with topological data analysis. *Astronomy & Astrophysics*, 648: A74, 2021. doi: 10.1051/0004-6361/202039048.

- Mathieu Carrière, Frédéric Chazal, Marc Glisse, Yuichi Ike, Hariprasad Kannan, and Yuhei Umeda. Optimizing persistent homology based functions. In *International Conference on Machine Learning*, pages 1294–1303. PMLR, 2021.
- Jacob Leygonie, Steve Oudot, and Ulrike Tillmann. A Framework for Differential Calculus on Persistence Barcodes. *Foundations of Computational Mathematics (FoCM)*, 22(4):1069–1131, August 2022a. ISSN 1615-3383. doi: 10.1007/s10208-021-09522-y.
- Kyle Cranmer, Johann Brehmer, and Gilles Louppe. The frontier of simulation-based inference. *Proceedings of the National Academy of Sciences*, 117(48):30055–30062, 2020. doi: 10.1073/pnas.1912789117.
- Alan F Heavens, Raul Jimenez, and Ofer Lahav. Massive lossless data compression and multiple parameter estimation from galaxy spectra. *Monthly Notices of the Royal Astronomical Society*, 317(4):965–972, 2000.
- Justin Alsing and Benjamin Wandelt. Generalized massive optimal data compression. *Monthly Notices of the Royal Astronomical Society: Letters*, 476(1):L60–L64, 2018. doi: 10.1093/mnrasl/sly029.
- Justin Alsing, Benjamin Wandelt, and Stephen Feeney. Massive optimal data compression and density estimation for scalable, likelihood-free inference in cosmology. *Monthly Notices of the Royal Astronomical Society*, 477(3):2874–2885, 2018.
- Tom Charnock, Guilhem Lavaux, and Benjamin D Wandelt. Automatic physical inference with information maximizing neural networks. *Physical Review D*, 97(8):083004, 2018.
- Peter Bubenik et al. Statistical topological data analysis using persistence landscapes. *J. Mach. Learn. Res.*, 16(1):77–102, 2015.
- Henry Adams, Tegan Emerson, Michael Kirby, Rachel Neville, Chris Peterson, Patrick Shipman, Sofya Chepushtanova, Eric Hanson, Francis Motta, and Lori Ziegelmeier. Persistence images: A stable vector representation of persistent homology. *Journal of Machine Learning Research*, 18(8): 1–35, 2017.
- Genki Kusano, Yasuaki Hiraoka, and Kenji Fukumizu. Persistence weighted gaussian kernel for topological data analysis. In *Proceedings of the 33rd International Conference on Machine Learning*, volume 48 of *Proceedings of Machine Learning Research*, pages 2004–2013. PMLR, 2016.
- Mathieu Carrière, Marco Cuturi, and Steve Oudot. Sliced Wasserstein Kernel for Persistence Diagrams. In Doina Precup and Yee Whye Teh, editors, *Proceedings of the 34th International Conference on Machine Learning (ICML 2017)*, volume 70, pages 664–673. PMLR, July 2017.
- Tam Le and Makoto Yamada. Persistence Fisher Kernel: A Riemannian Manifold Kernel for Persistence Diagrams. In Samy Bengio, Hanna Wallach, Hugo Larochelle, Kristen Grauman, Nicolò Cesa-Bianchi, and Roman Garnett, editors, *Advances in Neural Information Processing Systems 31 (NeurIPS 2018)*, volume 31. Curran Associates, Inc., 2018.
- Mathieu Carrière, Frédéric Chazal, Yuichi Ike, Théo Lacombe, Martin Royer, and Yuhei Umeda. Perslay: A neural network layer for persistence diagrams and new graph topological signatures. In *International Conference on Artificial Intelligence and Statistics*, pages 2786–2796. PMLR, 2020.
- Christoph Hofer, Roland Kwitt, Marc Niethammer, and Andreas Uhl. Deep learning with topological signatures. In *Advances in Neural Information Processing Systems*, volume 30, 2017.
- Rickard Brüel Gabriëlsson, Bradley J Nelson, Anjan Dwaraknath, and Primoz Skraba. A topology layer for machine learning. In *International Conference on Artificial Intelligence and Statistics*, pages 1553–1563. PMLR, 2020.
- Christoph Hofer, Florian Graf, Bastian Rieck, Marc Niethammer, and Roland Kwitt. Graph filtration learning. In *Proceedings of the 37th International Conference on Machine Learning*, volume 119 of *Proceedings of Machine Learning Research*, pages 4314–4323. PMLR, 2020.

- Jacob Leygonie, Gregory Henselman-Petrusek, and Steve Oudot. A framework for differential calculus on persistence barcodes. In *Foundations of Computational Mathematics*, volume 22, pages 1069–1130. Springer, 2022b.
- Olympio Hacquard, Krishnakumar Balasubramanian, Gilles Blanchard, Clément Levrard, and Wolfgang Polonik. Topologically Penalized Regression on Manifolds. *Journal of Machine Learning Research (JMLR)*, 23(161):1–39, 2022. ISSN 1533-7928.
- Felix Hensel, Michael Moor, and Bastian Rieck. A survey of topological machine learning methods. *Frontiers in Artificial Intelligence*, 4:681108, 2021.
- Pratyush Pranav, Herbert Edelsbrunner, Rien van de Weygaert, Gert Vegter, Michael Kerber, Bernard J. T. Jones, and Mathijs Wintraecken. The topology of the cosmic web in terms of persistent betti numbers. *Monthly Notices of the Royal Astronomical Society*, 465(4):4281–4310, 2017. doi: 10.1093/mnras/stw2862.
- Pratyush Pranav, Rien van de Weygaert, Gert Vegter, Bernard J T Jones, Robert J Adler, Job Feldbrugge, Changbom Park, Thomas Buchert, and Michael Kerber. Topology and geometry of gaussian random fields i: on betti numbers, euler characteristic, and minkowski functionals. *Monthly Notices of the Royal Astronomical Society*, 485(3):4167–4208, 05 2019. ISSN 0035-8711. doi: 10.1093/mnras/stz541. URL <https://doi.org/10.1093/mnras/stz541>.
- Sven Heydenreich, Benjamin Brück, Pierre Burger, Joachim Harnois-Déraps, Sandra Unruh, Tiago Castro, Klaus Dolag, and Nicolas Martinet. Persistent homology in cosmic shear. II. A tomographic analysis of DES-Y1. *A&A*, 667:A125, November 2022. doi: 10.1051/0004-6361/202243868.
- Jacky H. T. Yip, Matteo Biagetti, Alex Cole, Karthik Viswanathan, and Gary Shiu. Cosmology with persistent homology: a fisher forecast. *Journal of Cosmology and Astroparticle Physics*, 2024(09): 034, 2024. doi: 10.1088/1475-7516/2024/09/034.
- Herbert Edelsbrunner and John L. Harer. *Computational Topology: An Introduction*. American Mathematical Society, January 2010a. ISBN 978-1-4704-6769-2.
- Steve Oudot. *Persistence Theory: From Quiver Representations to Data Analysis*, volume 209 of *Mathematical Surveys and Monographs*. American Mathematical Society, 2015. ISBN 978-1-4704-3443-4.
- R.A. Fisher. *Statistical methods for research workers*. Edinburgh Oliver & Boyd, 1925.
- Maurice Kendall and Alan Stuart. *The advanced theory of statistics. Vol.2: Inference and relationship*. 1979.
- Erich Leo Lehmann and George Casella. *Theory of point estimation*. Springer, 1998.
- Thomas M. Cover and Joy A. Thomas. *Elements of Information Theory 2nd Edition (Wiley Series in Telecommunications and Signal Processing)*. Wiley-Interscience, July 2006. ISBN 0471241954.
- A. W. van der Vaart. *Asymptotic Statistics*. Cambridge Series in Statistical and Probabilistic Mathematics. Cambridge University Press, 1998.
- Frédéric Chazal, Brittany Terese Fasy, Fabrizio Lecci, Alessandro Rinaldo, and Larry Wasserman. Stochastic Convergence of Persistence Landscapes and Silhouettes. In *Proceedings of the 30th Annual Symposium on Computational Geometry (SoCG 2014)*, SOCG’14, pages 474–483. Association for Computing Machinery, 2014. ISBN 978-1-4503-2594-3. doi: 10.1145/2582112.2582128.
- Martin Kilbinger. Cosmology with cosmic shear observations: A review. *Reports on Progress in Physics*, 78(8):086901, 2015.
- Dezso Ribli, Bálint Ármán Pataki, José Manuel Zorrilla Matilla, Daniel Hsu, Zoltán Haiman, and István Csabai. Weak lensing cosmology with convolutional neural networks on noisy data. *MNRAS*, 490(2):1843–1860, December 2019. doi: 10.1093/mnras/stz2610.
- Sihao Cheng, Yuan-Sen Ting, Brice Ménard, and Joan Bruna. A new approach to observational cosmology using the scattering transform. *Monthly Notices of the Royal Astronomical Society*, 499(4):5902–5914, 2020.

- Erwan Allys, Titouan Marchand, Jean-François Cardoso, Francisco Villaescusa-Navarro, Shirley Ho, and Stéphane Mallat. New interpretable statistics for large-scale structure analysis and generation. *Physical Review D*, 102(10):103506, 2020.
- Florian List, Noemi Anau Montel, and Christoph Weniger. Bayesian Simulation-based Inference for Cosmological Initial Conditions. *arXiv e-prints*, art. arXiv:2310.19910, October 2023. doi: 10.48550/arXiv.2310.19910.
- Angel Villar-Corrales and Veniaming I. Morgenshtern. Scattering transform based image clustering using projection onto orthogonal complement. In *Proceedings of the 2021 ACM Workshop on Intelligent Cross-Data Analysis and Retrieval, ICDAR '21*, page 24–32, New York, NY, USA, 2021. Association for Computing Machinery. ISBN 9781450385299. doi: 10.1145/3463944.3469098. URL <https://doi.org/10.1145/3463944.3469098>.
- James R. Munkres. *Elements of Algebraic Topology*. CRC Press, 1st edition edition, 1984. ISBN 978-0-367-09141-5.
- Herbert Edelsbrunner and John Harer. *Computational topology: an introduction*. American Mathematical Soc., 2010b.
- J Hartlap, P Simon, and P Schneider. Why your model parameter confidences may be too optimistic. unbiased estimation of the inverse covariance matrix. *Astronomy & Astrophysics*, 464(1):399–404, 2007.
- Roger A Horn and Charles R Johnson. *Matrix analysis*. Cambridge university press, 2012.
- Steven M Kay. Fundamentals of statistical signal processing: estimation theory. *Prentice Hall*, 1: Chapter–3, 1997.
- George Papamakarios and Iain Murray. Fast ε -free inference of simulation models with bayesian conditional density estimation. In *Advances in Neural Information Processing Systems 29 (NIPS 2016)*, Advances in Neural Information Processing Systems, pages 1028–1036. Neural Information Processing Systems Foundation, Inc, December 2016. URL <https://nips.cc/Conferences/2016>. 30th Annual Conference on Neural Information Processing Systems, NIPS 2016 ; Conference date: 05-12-2016 Through 10-12-2016.
- Jan-Matthis Lueckmann, Pedro J. Gonçalves, Giacomo Bassetto, Kaan Öcal, Marcel Nonnenmacher, and Jakob H. Macke. Flexible statistical inference for mechanistic models of neural dynamics. In *Proceedings of the 31st International Conference on Neural Information Processing Systems, NIPS'17*, page 1289–1299, Red Hook, NY, USA, 2017. Curran Associates Inc. ISBN 9781510860964.
- David S. Greenberg, Marcel Nonnenmacher, and Jakob H. Macke. Automatic posterior transformation for likelihood-free inference. In *International Conference on Machine Learning*, 2019. URL <https://api.semanticscholar.org/CorpusID:159041084>.
- Laurent Dinh, Jascha Sohl-Dickstein, and Samy Bengio. Density estimation using real NVP. In *International Conference on Learning Representations*, 2017. URL <https://openreview.net/forum?id=HkpbnH9lx>.
- Nicolas Martinet, Joachim Harnois-Déraps, Eric Jullo, and Peter Schneider. Probing dark energy with tomographic weak-lensing aperture mass statistics. *Astronomy & Astrophysics*, 646:A62, February 2021. doi: 10.1051/0004-6361/202039679.
- Marika Asgari and Peter Schneider. A new data compression method and its application to cosmic shear analysis. *Astronomy & Astrophysics*, 578:A50, June 2015. doi: 10.1051/0004-6361/201424905.
- Mathieu Andreux, Tomàs Angles, Georgios Exarchakis, Roberto Leonarduzzi, Gaspar Rochette, Louis Thiry, John Zarka, Stéphane Mallat, Joakim Andén, Eugene Belilovsky, Joan Bruna, Vincent Lostanlen, Muawiz Chaudhary, Matthew J. Hirn, Edouard Oyallon, Sixin Zhang, Carmine Cella, and Michael Eickenberg. Kymatio: Scattering transforms in python. *Journal of Machine Learning Research*, 21(60):1–6, 2020. URL <http://jmlr.org/papers/v21/19-047.html>.

A Persistent homology: preliminaries

A key component of our summary statistic, the persistence diagram, is defined through the theory of persistent homology. In this section, we recall the basics of homology groups and persistence theory.

Simplicial homology. In this section, we briefly review the fundamentals of simplicial homology with coefficients in $\mathbb{Z}/2\mathbb{Z}$, which is the setting adopted for practical computations. For a more comprehensive introduction, we refer the reader to [Munkres, 1984, Chapter 1]. The basic building blocks of simplicial (persistent) homology are *simplicial complexes*, which provide combinatorial representations of topological spaces that can be efficiently manipulated algorithmically.

Definition A.1. Given a finite set of points $X_n := \{x_1, \dots, x_n\}$ sampled from a topological space X , an *abstract simplicial complex* constructed from X_n is a collection $S(X_n)$ of subsets of X_n such that:

- if $\tau \in S(X_n)$ and $\sigma \subseteq \tau$, then $\sigma \in S(X_n)$, and
- if $\sigma, \tau \in S(X_n)$, then either $\sigma \cap \tau \in S(X_n)$ or $\sigma \cap \tau = \emptyset$.

Each element $\sigma \in S(X_n)$ is called a *simplex*, and its *dimension* is defined by $\dim(\sigma) := \text{card}(\sigma) - 1$. Simplices of dimension 0 are referred to as *vertices*.

A central operator in simplicial homology is the *boundary operator*, which maps a simplex to the formal sum of its faces. Such formal sums are called *chains*, and the collection of chains forms a group, denoted by $Z_*(S(X_n))$.

Definition A.2. Given a simplex $\sigma = [x_{i_1}, \dots, x_{i_p}]$, the boundary operator ∂ is defined as

$$\partial(\sigma) := \sum_{j=1}^p [x_{i_1}, \dots, x_{i_{j-1}}, x_{i_{j+1}}, \dots, x_{i_p}].$$

In other words, $\partial(\sigma)$ is obtained by removing one vertex at a time from σ . This definition extends linearly to arbitrary chains.

A topological feature is represented by a *cycle*, that is, a chain whose boundary vanishes. Working over $\mathbb{Z}/2\mathbb{Z}$, this condition corresponds to requiring that each simplex in the boundary appears an even number of times, so that duplicates cancel out. Formally, a chain c is a cycle if $\partial(c) = 0$.

It follows directly that $\partial \circ \partial = 0$, meaning that the boundary of any chain is itself a cycle. However, cycles that arise as boundaries of higher-dimensional chains are considered *trivial*, and should be excluded. The set of such chains forms a subgroup denoted by $B_*(S(X_n))$.

Definition A.3. The k -th homology group is defined as the quotient

$$H_k(S(X_n)) := \frac{Z_k(S(X_n))}{B_k(S(X_n))}.$$

Equivalently, $H_k(S(X_n))$ consists of equivalence classes of k -dimensional cycles modulo boundaries. In fact, when working over $\mathbb{Z}/2\mathbb{Z}$, this group is a vector space.

Hence, homology groups are vector spaces computed on simplicial complexes built on finite data sets, and whose bases encode the different cycles of the complex which are not boundaries. Intuitively, these cycles represent topological features, whose types depend on the homology group degree: connected components ($k = 0$), loops ($k = 1$), cavities ($k = 2$), and their higher-dimensional counterparts ($k > 2$). In practice, simplicial complexes can be built on (a) point clouds with the so-called Vietoris-Rips complexes $V_\delta(X_n)$ (by creating simplices whose corresponding vertices are points that are all at distance at most δ from each other), and (b) images with the so-called cubical complexes $C(I)$ (by creating simplices whose corresponding vertices are neighboring pixels).

Persistent homology. The core objective of persistent homology is to extract *persistent* topological information from *filtrations*, i.e., sequences of growing simplicial complexes.

Definition A.4. Let $S = S(X_n)$ be a finite simplicial complex. A *filtration* of S is a family $(S_t)_t$ of subcomplexes such that $S_p \subseteq S_q$ whenever $p \leq q$. For each simplex $\sigma \in S$, define its *insertion time*, or *filtration value*, as $t(\sigma) := \inf\{t \mid \sigma \in S_t\}$.

From a topological viewpoint, the addition of a simplex σ to the filtration produces exactly one of two effects: either it gives rise to a new topological feature (for instance, inserting an edge may create a loop), hence increasing the dimension of the homology group in degree $\dim(\sigma)$ of the subcomplex, or it eliminates an existing feature of lower dimension (for example, connecting two previously disjoint components), hence decreasing the dimension of the homology group in degree $\dim(\sigma) - 1$. Using a matrix reduction algorithm that leverages the vector space structure of homology groups [Edelsbrunner and Harer, 2010b, §IV.2], persistent homology associates to each feature a *critical pair* of simplices (σ_b, σ_d) corresponding to its creation and destruction, together with the associated *birth* and *death* times $t(\sigma_b)$ and $t(\sigma_d)$.⁴

Definition A.5. The resulting collection of intervals $(t(\sigma_b), t(\sigma_d))$ in homological dimension k forms a finite subset of the half-plane $\{(b, d) \in \mathbb{R}^2 \mid b < d\}$ known as the k -*persistence diagram* (PD) of the filtration $(S_t)_t$. The quantity $\frac{1}{\sqrt{2}}|t(\sigma_b) - t(\sigma_d)|$, corresponding to the distance to the diagonal $\{b = d\}$, is called the *persistence* of the feature and measures how long it remains detectable across scales.

In the case of Vietoris-Rips complexes, it is common to build filtrations $\{V_\delta(X_n)\}_{\delta>0}$ by letting their corresponding neighborhood threshold δ increase, and in the case of images, it is common to use the growing sublevel sets of the pixel value function $\{f^{-1}((-\infty, \alpha])\}_{\alpha \in \mathbb{R}}$, where an image P is represented as a function $f : P \rightarrow \mathbb{R}$ valued on the grid P of pixels.

Very importantly, PDs are *stable* [Cohen-Steiner et al., 2007]: when computed from the sublevel sets of two continuous functions f, g defined on the same space, PDs can be compared with the so-called bottleneck distance d_b (which is similar to an optimal transport metric).

Definition A.6 (bottleneck distance). Let Dgm and Dgm' be two PDs. The *bottleneck distance* d_b between PDs is defined as:

$$d_b(\text{Dgm}, \text{Dgm}') := \inf_{P \in \mathcal{P}(\text{Dgm}, \text{Dgm}')} c(P), \quad (6)$$

where $\mathcal{P}(\text{Dgm}, \text{Dgm}')$ denotes the set of *partial correspondences*, i.e., the set of subsets of $\text{Dgm} \times \text{Dgm}'$ s.t. the first and second projections $\pi_1 : (p, p') \mapsto p$ and $\pi_2 : (p, p') \mapsto p'$ are injective, and where the *cost* of a partial correspondence P is defined as:

$$c(P) := \max\left\{ \max_{(p, p') \in P} \|p - p'\|_\infty, \max_{p \notin \text{im}(\pi_1)} \|p - \pi_\Delta(p)\|_\infty, \max_{p' \notin \text{im}(\pi_2)} \|p' - \pi_\Delta(p')\|_\infty \right\}. \quad (7)$$

Then, the main result of PH states that:

$$d_b(\text{Dgm}_k(f), \text{Dgm}_k(g)) \leq \|f - g\|_\infty.$$

Vectorizations and Differentiability. Finally, PDs are often represented by vectors to make amenable to standard computations (addition, inner product, etc).

Definition A.7. A *vectorization* of PDs is a continuous function $\varphi : \mathcal{D} \rightarrow \mathcal{H}$, where \mathcal{D} is the space of PDs, and \mathcal{H} is a Hilbert space.

Common representations include, e.g., the persistence landscape Bubenik et al. [2015], the persistence image Adams et al. [2017], and neural network-based vectorizations such as PersLay Carrière et al. [2020]. Finally, a recent property of PDs is their *differentiability*: as every PD point is associated to a critical pair, the map $f \mapsto \text{Dgm}_k(f)$ is piecewise smooth in f . Indeed, as the critical pairs only depend on the filtration order, the combinatorial pairing is locally constant, and PDs can be built locally by picking the insertion times at the critical pair indices in the filtration. This gather-based strategy (described initially in Carrière et al. [2021]) can be used in a gradient descent optimization scheme based on backpropagation by computing the critical pairs once in the forward pass and reading the filtration values off the input tensor through differentiable indexing on the backward pass.

B More details on Fisher estimation

We estimate the Gaussian Fisher loss $F_\phi^G(\theta_{\text{fid}})$ at fiducial parameter with structured batches \mathcal{B} . A batch \mathcal{B} includes realizations at θ_{fid} to estimate Σ_ϕ via sample covariance, to which we apply the Hartlap

⁴Some features may never be destroyed; in that case, their death time is set to $+\infty$.

correction [Hartlap et al., 2007] for unbiasedness of the precision matrix, as well as realizations at infinitesimal perturbations around θ_{fid} to compute $J_\theta \mu_\phi(\theta_{\text{fid}})$ via central finite differences. These empirical estimates, denoted as $\widehat{\Sigma}_{\phi, \mathcal{B}}$ and $\widehat{J}_{\theta, \mathcal{B}}$ respectively, are combined to evaluate the Fisher matrix through the quadratic form:

$$\widehat{F}_{\phi, \mathcal{B}}^G(\theta_{\text{fid}}) = \widehat{J}_{\theta, \mathcal{B}}^\top \widehat{P}_{\phi, \mathcal{B}} \widehat{J}_{\theta, \mathcal{B}}, \quad (8)$$

where $\widehat{P} = \frac{n_s - M - 2}{n_s - 1} \widehat{\Sigma}^{-1}$ with the condition $n_s > M + 2$ represents the Hartlap-corrected precision matrix.

The validity of this estimator relies on two key assumptions: the local linearity of the summary response and its Gaussianity. Since finite differences are only valid in a locally linear regime, we check this assumption by repeating the derivative estimate at two step sizes and verifying that the derivatives, and the resulting Fisher matrices, are stable.

Furthermore, we validate the Gaussian approximation of the final summaries with Kolmogorov–Smirnov (KS) tests. Specifically, we apply a 1D KS test to each component of the compressed summary against a Gaussian with matching mean and variance; at a significance level of $\alpha = 0.05$, we find the summaries to be consistent with the Gaussian assumption.

MOPED Compression. To compress the output of the vectorization map V_ϕ into a reduced space \mathbb{R}^M , one elegant choice is MOPED compression [Heavens et al., 2000]. This is a linear operator defined by a matrix $C_\phi \in \mathbb{R}^{d \times \dim(V_\phi)}$ given by $C_\phi = [J_\theta \tilde{\mu}_\phi(\theta_{\text{fid}})]^\top \tilde{\Sigma}_\phi^{-1}(\theta_{\text{fid}})$, where $\tilde{\mu}_\phi(\theta)$ and $\tilde{\Sigma}_\phi(\theta)$ are the mean and covariance of the vectorization output evaluated at θ . In our implementation, $J_\theta \tilde{\mu}_\phi(\theta_{\text{fid}})$ and $\tilde{\Sigma}_\phi(\theta_{\text{fid}})$ are estimated using a portion of the batch \mathcal{B} and we evaluate the final Fisher information on the remaining part. In practice, the Jacobian $J_\theta \tilde{\mu}_\phi(\theta_{\text{fid}})$ is estimated via finite differences, the inverse covariance estimated from $\tilde{\Sigma}_\phi(\theta_{\text{fid}})$ is corrected using the Hartlap factor. Under the Gaussian assumption of the vectorization output, MOPED is provably lossless, ensuring the Fisher information of the resulting d -dimensional summaries ($M = d$) matches the information content of the full vector.

C Proof of the Stability Theorem

The proof proceeds in three steps: we first establish local Lipschitz continuity of $\phi \mapsto \Sigma_\phi^{-1}$ (Proposition C.1), then of $\phi \mapsto F_\phi(\theta_{\text{fid}})$ (Proposition C.2), and finally of $\mathcal{L} = -\log |\det F|$. The last step relies on a standard perturbation bound for the log-determinant of a positive-definite matrix, combined with Weyl’s inequality to ensure $F_\phi(\theta_{\text{fid}}) + t \Delta F$ stays uniformly away from singular along the segment $t \in [0, 1]$. For the sake of brevity, throughout this Appendix we write $J_\phi := J_\theta \mu_\phi(\theta_{\text{fid}})$ and $F_\phi := F_\phi^G$.

Proposition C.1. *Let $s_\phi: \mathcal{X} \rightarrow \mathbb{R}^d$ satisfy Assumptions 3.1(i)–(iii). Let $\varepsilon := \|\phi' - \phi\|$ and $\delta_\Sigma := 4L_s M \varepsilon$. If $\kappa_\Sigma \delta_\Sigma < 1$, then*

$$\|\Sigma_{\phi'}^{-1} - \Sigma_\phi^{-1}\|_{\text{op}} \leq \frac{\kappa_\Sigma^2 \delta_\Sigma}{1 - \kappa_\Sigma \delta_\Sigma}. \quad (9)$$

In particular, $\phi \mapsto \Sigma_\phi^{-1}$ is locally Lipschitz.

Proof. We first bound $\|\Sigma_\phi - \Sigma_{\phi'}\|_{\text{op}}$. For ease of notation, given $\phi, \phi' \in \Phi$, we write $v = s_\phi(X)$, $v' = s_{\phi'}(X)$, $\mu = \mu_\phi(\theta_{\text{fid}})$, $\mu' = \mu_{\phi'}(\theta_{\text{fid}})$. Since $\Sigma_\phi = \mathbb{E}[vv^\top] - \mu\mu^\top$, it holds that

$$\Sigma_\phi - \Sigma_{\phi'} = (\mathbb{E}[vv^\top] - \mathbb{E}[v'(v')^\top]) - (\mu\mu^\top - \mu'\mu'^\top).$$

Let us focus on the right-hand side of the equation. For the first term, we have the identity

$$vv^\top - v'(v')^\top = (v - v')v^\top + v'(v - v')^\top.$$

In expectation, taking operator norms and using the triangle inequality,

$$\|\mathbb{E}[vv^\top] - \mathbb{E}[v'(v')^\top]\|_{\text{op}} \leq \mathbb{E}[\|v - v'\| \|v\|] + \mathbb{E}[\|v'\| \|v - v'\|].$$

By (i), $\|v - v'\| \leq L_s \varepsilon$ pointwise, so this factors out of both expectations. By Jensen's inequality and (ii), $\mathbb{E}[\|v\|] \leq (\mathbb{E}[\|v\|^2])^{1/2} \leq M$, and similarly $\mathbb{E}[\|v'\|] \leq M$. Therefore

$$\|\mathbb{E}[vv^\top] - \mathbb{E}[v'(v')^\top]\|_{\text{op}} \leq 2L_s M \varepsilon. \quad (10)$$

For the second term, the same identity gives

$$\mu\mu^\top - \mu'(\mu')^\top = (\mu - \mu')\mu^\top + \mu'(\mu - \mu')^\top,$$

so that

$$\|\mu\mu^\top - \mu'(\mu')^\top\|_{\text{op}} \leq \|\mu - \mu'\| \|\mu\| + \|\mu'\| \|\mu - \mu'\|.$$

By the same reasoning as for the first term,

$$\|\mu\mu^\top - \mu'(\mu')^\top\|_{\text{op}} \leq 2L_s M \varepsilon. \quad (11)$$

By (10) and (11), using the triangle inequality, we get that

$$\|\Sigma_\phi - \Sigma_{\phi'}\|_{\text{op}} \leq 4L_s M \varepsilon =: \delta_\Sigma. \quad (12)$$

Since $\kappa_\Sigma \delta_\Sigma < 1$ by hypothesis, the matrix $\Sigma_{\phi'}$ is invertible and the resolvent identity $\Sigma_{\phi'}^{-1} - \Sigma_\phi^{-1} = -\Sigma_{\phi'}^{-1}(\Sigma_{\phi'} - \Sigma_\phi)\Sigma_\phi^{-1}$, combined with a Neumann series bound on $\|\Sigma_{\phi'}^{-1}\|_{\text{op}}$ (see e.g. Horn and Johnson [2012], Corollary 5.6.16), yields the statement. \square

Proposition C.2. *Let $F_\phi(\theta_{\text{fid}}) = J_\phi^\top \Sigma_\phi^{-1} J_\phi$ be the Fisher information matrix as in Equation (3). Under Assumptions 3.1(i)–(iv), it holds that $\phi \mapsto F_\phi(\theta_{\text{fid}})$ is locally Lipschitz on Φ . More precisely, for all $\phi, \phi' \in \Phi$ with $\varepsilon := \|\phi' - \phi\|$ satisfying $\kappa_\Sigma \delta_\Sigma < 1$, where $\delta_\Sigma = 4L_s M \varepsilon$, it holds that*

$$\|F_{\phi'}(\theta_{\text{fid}}) - F_\phi(\theta_{\text{fid}})\|_{\text{op}} \leq \kappa_\Sigma L_J \varepsilon (2\|J_\phi\|_{\text{op}} + L_J \varepsilon) + \frac{\kappa_\Sigma^2 \delta_\Sigma}{1 - \kappa_\Sigma \delta_\Sigma} (\|J_\phi\|_{\text{op}} + L_J \varepsilon)^2.$$

Proof. For ease of notation, let $\varepsilon := \|\phi' - \phi\|$, $P := \Sigma_\phi^{-1}$, $P' := \Sigma_{\phi'}^{-1}$, $J := J_\phi$, $J' := J_{\phi'}$, $\Delta J := J' - J$, and $\Delta P := P' - P$. We have that

$$\begin{aligned} F_{\phi'}(\theta_{\text{fid}}) - F_\phi(\theta_{\text{fid}}) &= J'^\top P' J' - J^\top P J \\ &= (J + \Delta J)^\top (P + \Delta P) (J + \Delta J) - J^\top P J \\ &= (J + \Delta J)^\top (P J + P \Delta J + \Delta P J + \Delta P \Delta J) - J^\top P J. \end{aligned}$$

Hence, we have that

$$\begin{aligned} F_{\phi'}(\theta_{\text{fid}}) - F_\phi(\theta_{\text{fid}}) &= J^\top P \Delta J + J^\top \Delta P J + J^\top \Delta P \Delta J + (\Delta J)^\top P J \\ &\quad + (\Delta J)^\top P \Delta J + (\Delta J)^\top \Delta P J + (\Delta J)^\top \Delta P \Delta J. \end{aligned}$$

We recall that $\|P\|_{\text{op}} \leq \kappa_\Sigma$ by hypothesis (iii), $\|\Delta J\|_{\text{op}} \leq L_J \varepsilon$ by hypothesis (iv), and $\|\Delta P\|_{\text{op}} \leq \kappa_\Sigma^2 \delta_\Sigma / (1 - \kappa_\Sigma \delta_\Sigma)$ by Proposition C.1. Hence, we get that

$$\|F_{\phi'}(\theta_{\text{fid}}) - F_\phi(\theta_{\text{fid}})\|_{\text{op}} \leq \kappa_\Sigma L_J \varepsilon (2\|J\|_{\text{op}} + L_J \varepsilon) + \frac{\kappa_\Sigma^2 \delta_\Sigma}{1 - \kappa_\Sigma \delta_\Sigma} (\|J\|_{\text{op}} + L_J \varepsilon)^2$$

whenever $\kappa_\Sigma \delta_\Sigma < 1$. In particular, $\phi \mapsto F_\phi(\theta_{\text{fid}})$ is locally Lipschitz. \square

We are now able to prove the main result.

Proof of Theorem 3.2. Let $\Delta F := F_{\phi'}(\theta_{\text{fid}}) - F_\phi(\theta_{\text{fid}})$ and define $g: [0, 1] \rightarrow \mathbb{R}$ by $g(t) := \log \det(F_\phi(\theta_{\text{fid}}) + t\Delta F)$. By Proposition C.2, whenever $4\kappa_\Sigma L_s M \varepsilon < 1$ there exists a constant $C_F > 0$ (depending on κ_Σ , L_s , M , L_J , and $\|J_\phi\|_{\text{op}}$) such that $\|\Delta F\|_{\text{op}} \leq C_F \varepsilon$. Set

$$\varepsilon_0(\phi) := \min \left\{ \frac{1}{4\kappa_\Sigma L_s M}, \frac{\lambda_{\min}(F_\phi(\theta_{\text{fid}}))}{C_F} \right\},$$

so that for $\varepsilon < \varepsilon_0(\phi)$ both Proposition C.2 applies and $\|\Delta F\|_{\text{op}} < \lambda_{\min}(F_\phi(\theta_{\text{fid}}))$. By Weyl's inequality for symmetric matrices, $\lambda_{\min}(F_\phi(\theta_{\text{fid}}) + t\Delta F) \geq \lambda_{\min}(F_\phi(\theta_{\text{fid}})) - t\|\Delta F\|_{\text{op}} > 0$ for all $t \in [0, 1]$, so $F_\phi(\theta_{\text{fid}}) + t\Delta F$ is positive definite along the segment and g is differentiable with

$$g'(t) = \text{tr}((F_\phi(\theta_{\text{fid}}) + t\Delta F)^{-1} \Delta F).$$

By the mean value theorem, $|\mathcal{L}(\phi') - \mathcal{L}(\phi)| = |g(1) - g(0)| \leq \sup_{t \in [0,1]} |g'(t)|$. Since $|\text{tr}(C)| \leq p \|C\|_{\text{op}}$ for any $C \in \mathbb{R}^{p \times p}$ and

$$\|(F_\phi(\theta_{\text{fid}}) + t\Delta F)^{-1}\Delta F\|_{\text{op}} \leq \frac{\|\Delta F\|_{\text{op}}}{\lambda_{\min}(F_\phi(\theta_{\text{fid}})) - \|\Delta F\|_{\text{op}}},$$

we obtain

$$|\mathcal{L}(\phi') - \mathcal{L}(\phi)| \leq \frac{p \|\Delta F\|_{\text{op}}}{\lambda_{\min}(F_\phi(\theta_{\text{fid}})) - \|\Delta F\|_{\text{op}}}. \quad (13)$$

Combining (13) with the bound $\|\Delta F\|_{\text{op}} \leq C_F \varepsilon$ from Proposition C.2 yields (5). \square

D Stability assumptions for TDA pipelines

In this appendix we verify that the pipelines used in Section 4 satisfy Assumptions 3.1(i)–(v) of Theorem 3.2. Recall that the summary map takes the form

$$s_\phi = C_\phi \circ V_\phi \circ \text{Dgm}_k \circ f_\phi,$$

as in Eq. (2). For non-topological pipelines (IMNN, MLP-only, GNN-only, $\log(C_\ell)$ +MOPED, peak counts, wavelet scattering), the persistence and diagram-vectorization stages collapse to the identity. For pipelines with no trainable parameters (Cubical-PI, Cubical-Silhouette, Cubical-Curves, $\log(C_\ell)$ +MOPED, peak counts, wavelet scattering, DTM), s_ϕ does not depend on ϕ , so Assumptions (i) and (iv) hold trivially with $L_s = 0$ and $L_J = 0$. We focus the verification on the components that introduce ϕ -dependence, and discuss (ii), (iii) and (v) for all pipelines, learnable or not. We present the verification for a single homological dimension k ; concatenating multiple dimensions, or multiple tomographic bins as in Section 4.3, preserves each assumption since each is closed under direct sum of summaries.

Assumption 3.1(i): Lipschitz continuity of s_ϕ in ϕ . The map $\phi \mapsto s_\phi(X)$ is a composition of stages, each Lipschitz in its input. We discuss the contribution of each stage in turn.

Filtrations. The fixed filtrations used in this work (the cubical filtration, the angular power spectrum used in the lensing baseline, and the DTM vertex function on the spiral) do not depend on ϕ and contribute a constant of zero to the Lipschitz constant. The learnable filtrations are neural networks: the per-point MLP g_ϕ and the GNN of Section 4.1, the small CNN prepended to the cubical filtration in TF-CNN-PersLay (Appendix J.2), and the strided CNN encoders used in the IMNN and in the non-TDA baselines MLP-only and GNN-only. Each of these is a finite composition of affine maps with Lipschitz activations (LeakyReLU, GELU); on a compact parameter set Φ and a bounded data domain K , the gradient $\nabla_\phi f_\phi(x)$ is uniformly bounded over $\Phi \times K$, so $\phi \mapsto f_\phi(x)$ is Lipschitz with a constant independent of x . The lower-star extension $f_\phi(e_{ij}) = \|x_i - x_j\| + \max\{f_\phi(x_i), f_\phi(x_j)\}$ used on the Alpha complex (Section 4.1), and analogously the extension to higher-dimensional simplices, is the sum of a ϕ -independent term and a max of ϕ -Lipschitz scalars, hence Lipschitz with the same constant as on vertices.

Persistent homology. The map $f \mapsto \text{Dgm}_k(f)$ is 1-Lipschitz with respect to the bottleneck distance on diagrams and the sup-norm on filtration values, by the bottleneck stability theorem of persistent homology Cohen-Steiner et al. [2007]. For non-topological pipelines this stage is the identity.

Vectorizations. The fixed vectorizations are Lipschitz with respect to standard distances on diagrams: persistence images are 1-Lipschitz in the 1-Wasserstein distance Adams et al. [2017]; persistence silhouettes with uniform weighting are Lipschitz in the ∞ -Wasserstein distance on bounded support, as means of 1-Lipschitz tent functions Bubenik et al. [2015]; the differentiable persistence curves of Section J.3 are sums of soft-sigmoid cumulative distribution functions, hence Lipschitz with constant $O(\tau^{-1})$ on bounded support (where τ is the soft-sigmoid temperature reported in Appendix J.3). The learnable vectorization PersLay applies a permutation-invariant set network with spectral normalization on every linear layer (Appendix J.3), which constrains each layer’s operator norm to at most one and yields a Lipschitz set network in W_1 on diagrams, with a constant uniformly bounded in ϕ . The identity vectorization used by the IMNN, $\log(C_\ell)$, peak counts, and wavelet scattering is trivially 1-Lipschitz. The non-topological baselines MLP-only and GNN-only end with sum-pooling over N points, which is Lipschitz with constant \sqrt{N} by Cauchy–Schwarz.

Compressors. The MOPED compressor is a fixed linear map at each gradient step. Its operator norm is bounded by the empirical operator norm of the C_ϕ estimate (defined in Appendix B), which is in turn controlled by the Hartlap correction and the condition-number monitoring described in Section 2. The periodic refit of MOPED every 50 steps (Appendix J.4) is treated as an external procedure and does not enter the within-step Lipschitz analysis. The MLP heads used as compressors on the spiral and in the pretrained TF-CNN-PersLay-MLP variant are Lipschitz on compact $\bar{\Phi}$ by the same neural network argument used for filtrations.

By composition, s_ϕ is Lipschitz in ϕ with constant L_s equal to the product of the stage-wise constants.

Assumption 3.1(ii): uniform second moment bound. All simulators used in this work produce data with bounded support or with bounded second moment: the spiral is supported on a square (Section 4.1); the GRF is a centered Gaussian field on a periodic grid with finite total variance (Section 4.2); the κ maps from `sbi_lens` have finite second moment after Gaussian smoothing (Section 4.3). Together with compactness of $\bar{\Phi}$ and the Lipschitz bound on s_ϕ from (i), this yields

$$M^2 := \sup_{\phi \in \bar{\Phi}} \mathbb{E}_{X \sim p(\cdot | \theta_{\text{fid}})} [\|s_\phi(X)\|^2] < \infty.$$

At the level of individual stages: bounded data yield bounded filtration values, hence persistence diagrams supported in a bounded region of \mathbb{R}^2 Cohen-Steiner et al. [2007]; the fixed vectorizations of Section J.3 (PI, silhouette, persistence curves) all map bounded diagrams to bounded vectors, and PersLay does so as well since spectral normalization keeps its outputs bounded under bounded inputs. The compressor preserves boundedness as the composition of either a bounded linear map (MOPED) or a Lipschitz MLP on compact $\bar{\Phi}$.

Assumption 3.1(iii): bound on $\|\Sigma_\phi^{-1}\|_{\text{op}}$. This assumption is verified empirically rather than by a structural argument on the pipeline. We rely on three diagnostics, run for every reported configuration: (a) the sample covariance is computed on a structured batch sized so that $n_s \gg M$ (Sections 4.1–4.3) and corrected by the Hartlap factor Hartlap et al. [2007] for unbiasedness of the precision matrix; (b) zero-variance features of the vectorization output are removed before inversion; (c) Gaussianity of the final summary is checked by per-component Kolmogorov–Smirnov tests at $\alpha = 0.05$ (Appendix B). In all reported runs, Σ_ϕ is invertible with bounded $\|\Sigma_\phi^{-1}\|_{\text{op}}$.

Assumption 3.1(iv): Lipschitz continuity of the Jacobian in ϕ . The Jacobian $J_\theta \mu_\phi(\theta_{\text{fid}})$ is estimated by centered finite differences with step sizes $\Delta = (\Delta_1, \dots, \Delta_d)$ specified in Appendix J.6. Under Assumption 3.1(i), Jensen’s inequality gives $\|\mu_{\phi'}(\theta) - \mu_\phi(\theta)\| \leq L_s \|\phi' - \phi\|$ for every θ in the stencil. Applying the triangle inequality column-wise to the finite-difference Jacobian and using $\|A\|_{\text{op}} \leq \|A\|_F$ then yields

$$L_J \leq \frac{2\sqrt{d}L_s}{\Delta_{\min}}, \quad \Delta_{\min} := \min_{i=1, \dots, d} \Delta_i.$$

Assumption 3.1(v): non-degeneracy of $F_\phi(\theta_{\text{fid}})$. Since Σ_ϕ^{-1} is positive definite by (iii), positive definiteness of $F_\phi(\theta_{\text{fid}}) = J_\theta \mu_\phi(\theta_{\text{fid}})^\top \Sigma_\phi^{-1} J_\theta \mu_\phi(\theta_{\text{fid}})$ is equivalent to $J_\theta \mu_\phi(\theta_{\text{fid}})$ having full column rank, i.e. the summary being sensitive to all d physical parameters at the fiducial. This is verified empirically in all reported configurations: the marginal uncertainties $\sigma(\theta_i) = (F_\phi^{-1})_{ii}^{1/2}$ reported in Sections 4.1–4.3 are finite and of the expected order of magnitude, and the condition number of F_ϕ is monitored throughout training (see (iii) above and the diagnostics in Appendix B).

E Noisy Spiral Total Fisher

This appendix derives the total Fisher information matrix for the 2D noisy spiral generative model. Points in \mathbb{R}^2 are sampled i.i.d. from a known two-component mixture, with a background component p_B and a spiral component p_S . Given a mixing weight $\lambda \in (0, 1)$, the point cloud $\mathcal{X} = \{x_k\}_{k=1}^N \subseteq \mathbb{R}^2$ is obtained by independently sampling each point from

$$p(x; \theta) = \lambda p_B(x) + (1 - \lambda) p_S(x; \theta), \quad (14)$$

where $\theta = (\mu, w)^\top$ are the target parameters: μ controls the radial expansion of the spiral and w its width. The background density p_B does not depend on θ and is uniform on a square $\mathcal{S} = [-h, h]^2$ of area $4h^2$. Since the spiral component p_S is most naturally expressed in polar coordinates (ρ, Φ) , with $x = \rho \cos \Phi$ and $y = \rho \sin \Phi$, we work in this system throughout. The Jacobian determinant of the change of variables is $|J| = \rho$, and in these coordinates the square \mathcal{S} is described by

$$\mathcal{S}' = \left\{ (\rho, \Phi) : 0 \leq \Phi < 2\pi, 0 \leq \rho \leq \frac{h}{\max(|\cos \Phi|, |\sin \Phi|)} \right\}. \quad (15)$$

The background density therefore reads

$$p_B(\rho, \Phi) = \frac{\rho}{4h^2} \mathbb{I}_{\mathcal{S}'}(\rho, \Phi), \quad (16)$$

where \mathbb{I}_A denotes the indicator function of the set A . Let us now focus on the spiral component p_S . The spiral is sampled hierarchically as follows:

1. an angular coordinate t is drawn uniformly on $[0, 4\pi)$, so that the spiral completes two full turns;
2. given t , the radial coordinate is perturbed by Gaussian noise, $\rho | t \sim \mathcal{N}(\mu t, w^2)$;
3. the sampled point is mapped to Cartesian coordinates via $(x, y) = (\rho \cos t, \rho \sin t)$.

Since t and $t + 2\pi$ map to the same point in \mathbb{R}^2 , to obtain an injective map we reparametrize the generative process on $\Phi \in [0, 2\pi)$ by marginalizing over the winding. Setting $\Phi := t \bmod 2\pi$, the two preimages $t \in \{\Phi, \Phi + 2\pi\}$ are equally likely conditionally on Φ , and the hierarchical sampling becomes $\Phi \sim \mathcal{U}(0, 2\pi)$, and $\rho | \Phi \sim \frac{1}{2} \mathcal{N}(\mu\Phi, w^2) + \frac{1}{2} \mathcal{N}(\mu(\Phi + 2\pi), w^2)$ ⁵. The spiral density therefore reads

$$p_S(\rho, \Phi | \theta) = \frac{1}{2\pi} \cdot \frac{1}{2\sqrt{2\pi}w} \left[\exp\left(-\frac{(\rho - \mu\Phi)^2}{2w^2}\right) + \exp\left(-\frac{(\rho - \mu(\Phi + 2\pi))^2}{2w^2}\right) \right] \mathbb{I}_{\mathcal{S}'}(\rho, \Phi), \quad (17)$$

supported on $\mathcal{S}'' = \{(\rho, \Phi) : 0 \leq \Phi < 2\pi, \rho \geq 0\}$. Since the sample is i.i.d. from $p(\cdot; \theta)$, the total Fisher information matrix in polar coordinates reads Kay [1997]

$$F_X[i, j](\theta) = N \iint \frac{\partial_{\theta_i} p(\rho, \Phi; \theta) \partial_{\theta_j} p(\rho, \Phi; \theta)}{p(\rho, \Phi; \theta)} d\rho d\Phi. \quad (18)$$

Since only p_S depends on θ , we have $\partial_{\theta} p = (1 - \lambda) \partial_{\theta} p_S$, and (18) specializes to

$$F_X[i, j](\theta) = N \iint \frac{(1 - \lambda)^2 \partial_{\theta_i} p_S \partial_{\theta_j} p_S}{\lambda p_B + (1 - \lambda) p_S} d\rho d\Phi, \quad (19)$$

where the dependence on (ρ, Φ, θ) has been suppressed for readability. To lighten the notation, we introduce $\zeta_1 = \frac{\rho - \mu\Phi}{w}$, $\zeta_2 = \frac{\rho - \mu(\Phi + 2\pi)}{w}$, and $g_\ell = \frac{1}{\sqrt{2\pi}w} e^{-\zeta_\ell^2/2}$ for $\ell = 1, 2$. A direct computation then yields

$$\partial_w p_S = \frac{1}{2\pi} \cdot \frac{1}{2} \left[g_1 \frac{\zeta_1^2 - 1}{w} + g_2 \frac{\zeta_2^2 - 1}{w} \right], \quad (20)$$

$$\partial_\mu p_S = \frac{1}{2\pi} \cdot \frac{1}{2} \left[g_1 \frac{\zeta_1 \Phi}{w} + g_2 \frac{\zeta_2 (\Phi + 2\pi)}{w} \right]. \quad (21)$$

The total Fisher information matrix $F_X(\theta)$ is then obtained by substituting (20)–(21) into (19). The resulting integral admits no known closed form and is evaluated numerically.

F Additional Noisy Spiral Results

We report the results for the spiral experiment for the other four fiducial parameter values in Table 4. In Figure 1 we plot the vertex values and the corresponding filtration learned by TF-TDA-MLP method.

Table 4: Complete spiral results for all fiducial configurations $(\mu_{\text{fid}}, w_{\text{fid}})$, averaged over 5 seeds. Entries are mean \pm standard deviation of $\log |F|$.

Method	(0.6, 0.1)	(0.8, 0.1)	(0.7, 0.2)	(0.5, 0.2)	(0.7, 0.3)
Total	24.27	24.24	21.36	21.41	19.64
<i>Fixed topological ablation: persistence without TopoFisher learning</i>					
DTM fixed filtration	17.18 \pm 0.06	16.34 \pm 0.25	15.83 \pm 0.09	16.65 \pm 0.06	15.16 \pm 0.05
<i>TopoFisher summaries: our learned topological contributions</i>					
TF-TDA-MLP	18.99 \pm 0.30	17.47 \pm 0.63	17.50 \pm 0.28	18.32 \pm 0.37	16.66 \pm 0.07
TF-TDA-GNN	16.20 \pm 0.19	15.57 \pm 0.37	15.14 \pm 0.14	16.63 \pm 0.43	14.72 \pm 0.11
<i>Unconstrained neural references: non-topological summaries</i>					
MLP-only	18.96 \pm 0.58	17.88 \pm 0.49	17.48 \pm 0.11	18.40 \pm 0.21	16.54 \pm 0.19
GNN-only	18.26 \pm 0.25	17.45 \pm 0.12	16.78 \pm 0.16	17.68 \pm 0.06	15.87 \pm 0.08

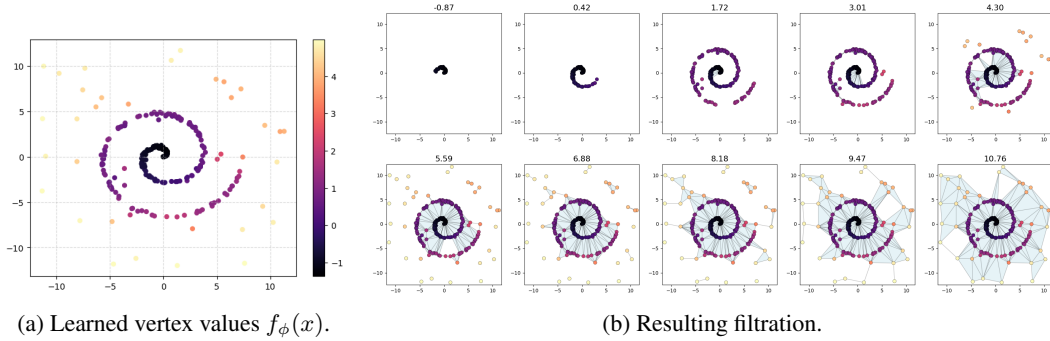


Figure 1: Visualization of the TF-TDA-MLP pipeline. (a) The model assigns filtration values to vertices to "unroll" the spiral geometry. (b) The corresponding filtration effectively prioritizes the manifold while filtering background noise.

To highlight the interpretability of the TF-TDA-MLP, we compare its learned filtration with the vertex mapping produced by the MLP-only baseline. Since the latter maps each point x to a two-dimensional statistic $f_\phi(x) \in \mathbb{R}^2$ before sum-pooling, we visualize both components in Fig. 2.

In contrast to the topological approach, the purely neural baseline lacks a clear geometric interpretation. The network appears to concentrate the information on a small subset of points that assume extreme values to drive the sum-pooling operation, but their spatial distribution does not correspond to identifiable features of the manifold.

G Total Fisher information for the GRF benchmark

Let $x \in \mathbb{R}^{N \times N}$ be a zero-mean isotropic and homogeneous Gaussian random field on a periodic grid, and let $\tilde{x}_{\mathbf{k}}$ denote its discrete Fourier coefficients. Under the simulator used in Section 4.2, the field is fully specified by the isotropic power spectrum

$$P(k; \theta) = A_s \left(\frac{k}{k_{\text{pivot}}} \right)^{-B}, \quad \theta = (A_s, B), \quad (22)$$

with $k = \|\mathbf{k}\|$ and k_{pivot} the geometric mean of the nonzero Fourier radii. Since the field is Gaussian with zero mean, the exact data likelihood is multivariate Gaussian with diagonal covariance $\Sigma(\theta)$ in Fourier space. The Fisher matrix is therefore

$$F_{ij}(\theta) = \frac{1}{2} \text{Tr}[\Sigma^{-1}(\theta) \partial_{\theta_i} \Sigma(\theta) \Sigma^{-1}(\theta) \partial_{\theta_j} \Sigma(\theta)]. \quad (23)$$

⁵The Gaussian conditional $\rho|\Phi$ places a small amount of mass on the region $\rho < 0$. For the fiducial $\mu = 0.6$, $w = 0.1$, this mass, concentrated near $\Phi \rightarrow 0^+$, is bounded by 10^{-2} and we neglect it in the following.

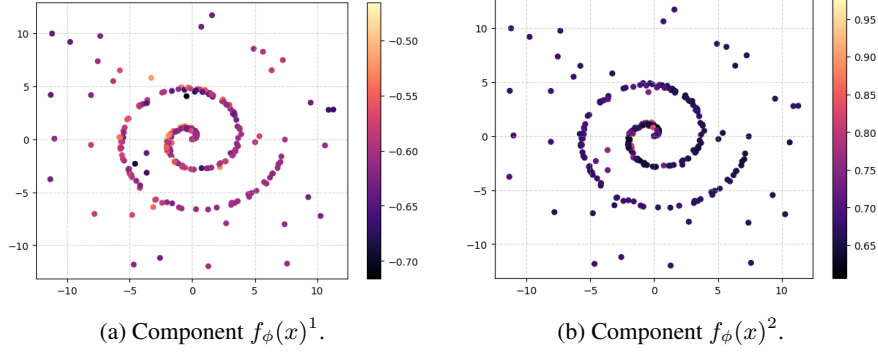


Figure 2: Vertex-wise outputs for the two components learned by the MLP-only baseline.

Because $\Sigma(\theta)$ is diagonal in the Fourier basis, Eq. (23) reduces to a sum over modes:

$$F_{ij}(\theta) = \frac{1}{2} \sum_{\mathbf{k} \neq 0} \frac{\partial_{\theta_i} P(k; \theta) \partial_{\theta_j} P(k; \theta)}{P(k; \theta)^2} = \frac{1}{2} \sum_{\mathbf{k} \neq 0} \partial_{\theta_i} \log P(k; \theta) \partial_{\theta_j} \log P(k; \theta). \quad (24)$$

Here the sum runs over all nonzero discrete Fourier modes of the $N \times N$ lattice; the prefactor $1/2$ accounts for the reality condition $\tilde{x}_{-\mathbf{k}} = \tilde{x}_{\mathbf{k}}^*$. Equivalently, one may sum only over an independent half-plane of modes and drop the factor $1/2$.

For the power-law spectrum used here,

$$\partial_{A_s} \log P(k; \theta) = \frac{1}{A_s}, \quad \partial_B \log P(k; \theta) = -\log\left(\frac{k}{k_{\text{pivot}}}\right). \quad (25)$$

Substituting into Eq. (24) gives

$$F_{A_s A_s} = \frac{1}{2A_s^2} \sum_{\mathbf{k} \neq 0} 1 = \frac{N_{\text{nz}}}{2A_s^2}, \quad (26)$$

$$F_{A_s B} = -\frac{1}{2A_s} \sum_{\mathbf{k} \neq 0} \log\left(\frac{k}{k_{\text{pivot}}}\right), \quad (27)$$

$$F_{BB} = \frac{1}{2} \sum_{\mathbf{k} \neq 0} \log^2\left(\frac{k}{k_{\text{pivot}}}\right), \quad (28)$$

where $N_{\text{nz}} = N^2 - 1$ is the number of nonzero Fourier modes.

The choice of pivot scale

$$k_{\text{pivot}} = \exp\left(\frac{1}{N_{\text{nz}}} \sum_{\mathbf{k} \neq 0} \log k\right) \quad (29)$$

makes the cross term vanish exactly:

$$\sum_{\mathbf{k} \neq 0} \log\left(\frac{k}{k_{\text{pivot}}}\right) = 0 \quad \implies \quad F_{A_s B} = 0. \quad (30)$$

Thus the total Fisher matrix is diagonal,

$$F(\theta) = \begin{pmatrix} \frac{N_{\text{nz}}}{2A_s^2} & 0 \\ 0 & \frac{1}{2} \sum_{\mathbf{k} \neq 0} \log^2\left(\frac{k}{k_{\text{pivot}}}\right) \end{pmatrix}. \quad (31)$$

Two useful consequences follow immediately. First, the bound is independent of the fiducial slope B_0 , since $\partial_B \log P$ does not depend on B . Second, the overall box-size normalization cancels in k/k_{pivot} , so only the discrete lattice of mode radii matters.

For our benchmark, $N = 64$, hence $N_{\text{nz}} = 64^2 - 1 = 4095$ and

$$F_{A_s A_s} = \frac{4095}{2} = 2047.5 \quad \implies \quad \sigma(A_s) = F_{A_s A_s}^{-1/2} = 0.0221. \quad (32)$$

The second diagonal entry is obtained by evaluating the lattice sum in Eq. (28) numerically on the nonzero 64×64 Fourier grid, yielding

$$F_{BB} \approx 5.16 \times 10^2, \quad \sigma(B) = F_{BB}^{-1/2} \approx 0.044. \quad (33)$$

Finally,

$$\log |F|_{\text{tot}} = \log(F_{A_s A_s} F_{BB}) \approx 13.89, \quad (34)$$

which is the denominator of efficiency used throughout Section 4.2.

H GRF: per- B results

This appendix reports the per-spectral-index results for the GRF benchmark of Section 4.2. All entries are computed at $N = 64$ and averaged over 5 independent seeds for each fiducial value $B \in \{-2, -1, 0, 1, 2\}$. The theoretical optimum is $\log |F_X| = 13.89$ for every value of B .

Table 5: GRF results for all spectral indices $B \in \{-2, -1, 0, 1, 2\}$, $N = 64$, averaged over 5 seeds. Entries are mean \pm standard deviation of $\log |F|$. The theoretical optimum is $\log |F_X| = 13.89$ for every B .

Method	$B = -2$	$B = -1$	$B = 0$	$B = 1$	$B = 2$
<i>Total</i>	<i>13.89</i>				
<i>Fixed topological ablations: persistence without TopoFisher learning</i>					
Cubical-PI	10.573 \pm 0.009	11.314 \pm 0.007	11.996 \pm 0.006	12.085 \pm 0.006	11.682 \pm 0.010
Cubical-Silhouette	9.895 \pm 0.012	10.597 \pm 0.012	11.304 \pm 0.005	11.256 \pm 0.005	10.369 \pm 0.010
Cubical-Curves	7.073 \pm 0.019	8.685 \pm 0.007	10.372 \pm 0.006	10.486 \pm 0.008	9.467 \pm 0.009
<i>TopoFisher summaries: our learned topological contributions</i>					
TF-Cubical-PersLay	13.011 \pm 0.013	12.880 \pm 0.003	12.756 \pm 0.007	12.520 \pm 0.005	11.980 \pm 0.008
TF-CNN-PersLay	11.920 \pm 0.120	12.078 \pm 0.081	12.189 \pm 0.081	12.205 \pm 0.046	11.936 \pm 0.103
<i>Unconstrained Fisher-neural reference: non-topological summary</i>					
IMNN	12.142 \pm 0.040	12.270 \pm 0.033	12.34 \pm 0.043	12.34 \pm 0.047	12.29 \pm 0.092

Table 6: GRF marginal uncertainties across spectral indices, averaged over 5 seeds. Each cell reports $\sigma(A_s)/\sigma(B)$. The theoretical values are $\sigma(A_s) = 0.022$ and $\sigma(B) = 0.044$ for every B .

Method	$B = -2$	$B = -1$	$B = 0$	$B = 1$	$B = 2$
<i>Total</i>	<i>0.022/0.044</i>				
<i>Fixed topological ablations: persistence without TopoFisher learning</i>					
Cubical-PI	0.0436/0.1445	0.0349/0.1049	0.0327/0.0759	0.0345/0.0690	0.0405/0.0723
Cubical-Silhouette	0.0529/0.1967	0.0381/0.1445	0.0349/0.1006	0.0411/0.0916	0.0625/0.1104
Cubical-Curves	0.1845/0.7144	0.0644/0.3410	0.0379/0.1480	0.0524/0.1190	0.0929/0.1376
<i>TopoFisher summaries: our learned topological contributions</i>					
TF-Cubical-PersLay	0.0284/0.0570	0.0287/0.0596	0.0298/0.0606	0.0325/0.0611	0.0380/0.0672
TF-CNN-PersLay	0.0334/0.0775	0.0339/0.0703	0.0335/0.0674	0.0333/0.0672	0.0356/0.0720
<i>Unconstrained Fisher-neural reference: non-topological summary</i>					
IMNN	0.0322/0.0693	0.0320/0.0657	0.0322/0.0636	0.0321/0.0639	0.0320/0.0636

I Further Lensing results

This appendix provides the per-bin and transfer-learning details for the weak lensing experiment of Section 4.3. All results use the $\sigma = 2'$ smoothed 512×512 convergence maps and the parameter pair

(Ω_m, σ_8) . For each tomographic bin and each method, we report the mean and standard deviation across 5 independent seeds. The per-bin quantities in Tables 7 are useful for diagnosing how information changes with source redshift, but the Survey-level constraints reported in the main text are obtained by adding the Fisher matrices across bins, and then computing $\log |F_{\text{tot}}|$ and $\sqrt{(F_{\text{tot}}^{-1})_{ii}}$.

Per-bin behavior. The per-bin log-determinants in Table 7 show three main trends. First, the standard $\log(C_\ell)$ baseline is comparatively flat across bins, with $\log |F| \simeq 10.2$ – 10.6 . Second, fixed topological summaries recover substantially more information than the power spectrum in the higher-redshift bins, where the lensing signal is stronger. Third, the learned diagram vectorization TF-Cubical-PersLay improves consistently over all fixed topological vectorizations and increases monotonically from bin 0 to bin 4, from $\log |F| = 16.71$ to $\log |F| = 18.99$. The unconstrained IMNN baseline is weaker in the first bin but becomes the strongest in the highest-redshift bins, reaching $\log |F| = 20.05$ in bin 4.

Table 7: Weak lensing per-bin results for (Ω_m, σ_8) at $\sigma = 2'$ smoothing. Each cell reports mean \pm standard deviation of $\log |F|$ across 5 seeds. Bin index increases with effective source redshift. Transfer rows are trained on lognormal maps and evaluated on LPT maps without retraining.

Method	bin 0	bin 1	bin 2	bin 3	bin 4
<i>External cosmology baseline</i>					
$\log(C_\ell)$ +MOPED	10.198 ± 0.086	10.574 ± 0.094	10.583 ± 0.080	10.499 ± 0.072	10.279 ± 0.069
<i>Fixed topological ablations: persistence without TopoFisher learning</i>					
Cubical-PI	12.672 ± 0.017	15.165 ± 0.025	16.055 ± 0.019	16.364 ± 0.020	16.346 ± 0.025
Cubical-Curves	8.935 ± 0.249	13.448 ± 0.074	14.912 ± 0.015	15.464 ± 0.014	15.296 ± 0.017
Cubical-Silhouette	13.048 ± 0.019	13.053 ± 0.020	12.673 ± 0.019	12.681 ± 0.016	13.259 ± 0.015
<i>TopoFisher summaries: our learned topological contributions</i>					
TF-Cubical-PersLay	16.705 ± 0.019	17.853 ± 0.012	18.286 ± 0.019	18.591 ± 0.032	18.988 ± 0.029
TF-CNN-PersLay	14.755 ± 0.133	17.166 ± 0.166	17.272 ± 0.608	17.171 ± 0.177	16.965 ± 0.514
<i>Unconstrained Fisher-neural reference: non-topological summary</i>					
IMNN	14.893 ± 0.097	17.624 ± 0.111	18.877 ± 0.051	19.694 ± 0.084	20.053 ± 0.091
<i>Transfer Fisher: lognormal-trained summaries evaluated on LPT maps</i>					
TF-Cubical-PersLay	10.785 ± 0.039	13.608 ± 0.014	16.565 ± 0.038	16.657 ± 0.019	17.011 ± 0.014
TF-CNN-PersLay	1.036 ± 1.292	5.863 ± 0.372	7.807 ± 0.638	9.508 ± 0.370	12.123 ± 2.380
IMNN	-8.519 ± 6.562	-2.030 ± 2.298	3.388 ± 2.321	2.601 ± 2.618	3.710 ± 1.623

Table 8: Weak lensing per-bin marginal uncertainties for in-distribution lognormal simulations. Each cell reports $\sigma(\Omega_m)/\sigma(\sigma_8)$ averaged over 5 seeds. These are per-bin constraints only; survey-level constraints are obtained by adding Fisher matrices across bins.

Method	bin 0	bin 1	bin 2	bin 3	bin 4
<i>External cosmology baseline</i>					
$\log(C_\ell)$	0.1242/0.1749	0.0975/0.1401	0.0866/0.1333	0.0788/0.1311	0.0712/0.1296
<i>Fixed topological ablations: persistence without TopoFisher learning</i>					
Cubical-PI	0.0848/0.0987	0.0481/0.0461	0.0344/0.0305	0.0299/0.0246	0.0246/0.0178
Cubical-Curves	0.4600/0.4873	0.0904/0.0826	0.0496/0.0421	0.0365/0.0291	0.0306/0.0234
Cubical-Silhouette	0.0837/0.0884	0.0783/0.0801	0.0778/0.0853	0.0676/0.0789	0.0442/0.0529
<i>TopoFisher summaries: our learned topological contributions</i>					
TF-Cubical-PersLay	0.0338/0.0410	0.0213/0.0227	0.0192/0.0198	0.0172/0.0183	0.0145/0.0168
TF-CNN-PersLay	0.0417/0.0424	0.0226/0.0183	0.0235/0.0163	0.0232/0.0145	0.0210/0.0132
<i>Unconstrained Fisher-neural reference: non-topological summary</i>					
IMNN	0.0449/0.0452	0.0219/0.0175	0.0157/0.0112	0.0119/0.0076	0.0097/0.0051

Transfer-learning diagnostic. The transfer experiment is intentionally stringent: all trainable components are optimized on the lognormal `sbi_lens` simulator and then evaluated without retraining on LPT-based maps at the same fiducial cosmology, resolution, and smoothing scale. The transfer degradation of the IMNN and TF-CNN-PersLay is large despite their strong in-distribution Fisher values, indicating that learned pixel-space neural stages can exploit simulator-specific features. In contrast, Cubical-PersLay has no learned pixel-space filtration and transfers much more reliably. Its transferred Fisher ellipse is still more degenerate than its in-distribution counterpart, as reflected by the weaker marginal uncertainties, but it preserves a high determinant and therefore a strong constraint along at least one cosmological parameter combination.

Details on simulation-based inference studies We perform simulation-based inference (also known as likelihood-free inference) using Neural Posterior Estimation [NPE; Papamakarios and Murray, 2016, Lueckmann et al., 2017, Greenberg et al., 2019]. Rather than approximating the intractable likelihood $p(d | \theta)$, NPE directly targets the posterior by training a conditional density estimator $q_\varphi(\theta | d)$, parameterised by neural-network weights φ , on simulated (θ, d) pairs drawn from the joint $p(\theta, d) = p(\theta)p(d | \theta)$.

We adopt a conditional normalizing flow as the density estimator, specifically a conditional RealNVP [Dinh et al., 2017] composed of a stack of affine coupling layers. In each coupling layer, the scale and shift parameters of the affine transformation are produced by a small MLP conditioner that takes as input both the masked half of the parameter vector and the conditioning summary statistic d .

Training proceeds by minimising the forward Kullback–Leibler divergence between the true posterior and the variational approximation,

$$\mathcal{L}(\varphi) = \mathbb{E}_{p(d)} [D_{\text{KL}}(p(\theta | d) || q_\varphi(\theta | d))], \quad (35)$$

which, up to a φ -independent constant, is equivalent to maximising the expected conditional log-likelihood of the flow on samples from the joint,

$$\varphi^* = \arg \max_{\varphi} \mathbb{E}_{p(\theta, d)} [\log q_\varphi(\theta | d)]. \quad (36)$$

We estimate this expectation by Monte Carlo over a training set of simulator draws. At inference time we condition the trained flow on the observed summary d_{obs} and draw samples directly from $q_{\varphi^*}(\theta | d_{\text{obs}})$.

We note that we perform our SBI using only auto-bins (i.e. correlations within the same bin). In principle, we could improve performance by including cross-correlations between different redshift bins [compare Martinet et al., 2021]. Likewise, in a realistic cosmological analysis we would compute the cross-correlation between all bin pairs in the power spectrum analysis. This is beyond the scope of demonstrating the feasibility of our TopoFisher pipeline, and uniformly disregarding cross-correlations between bins ensures a fair comparison between summary statistics. We reserve a more realistic lensing optimization that includes cross-correlations between bins for future work. We also note that the SBI posteriors of the Power Spectrum marginally exceed its previously computed Fisher information. This is due to the MOPED compression, which is lossless in theory, but imparts losses when the derivatives and covariance are noisy [Asgari and Schneider, 2015].

We show the inference constraints on our two-parameter scenario in Figure 3, and for the extended 6-parameter inference in Figure 4. The Ω_m in the main text is $\Omega_m = \Omega_c + \Omega_b$; the total matter density is the sum of the dark matter and baryonic matter densities. The prior over cosmological parameters used during SBI training is

$$\begin{aligned} \Omega_c &\sim \mathcal{N}_{>0}(0.2664, 0.2^2), \\ \Omega_b &\sim \mathcal{N}(0.0492, 0.006^2), \\ \sigma_8 &\sim \mathcal{N}(0.831, 0.14^2), \\ h_0 &\sim \mathcal{N}(0.6727, 0.063^2), \\ n_s &\sim \mathcal{N}(0.9645, 0.08^2), \\ w_0 &\sim \mathcal{N}_{[-2.0, -0.3]}(-1.0, 0.9^2), \end{aligned}$$

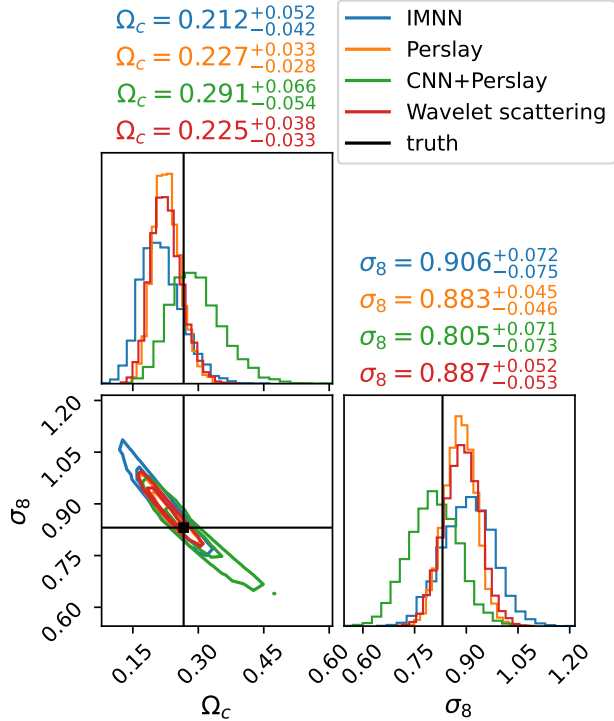


Figure 3: Comparison of SBI constraints from different summary statistics. The contours show the 1- and 2- σ uncertainties of the different models.

where $\mathcal{N}_{>0}$ denotes a half-normal (truncated at zero) and $\mathcal{N}_{[a,b]}$ a normal truncated to $[a, b]$. The reference (fiducial) cosmology is the truth value of each parameter: $(\Omega_c, \Omega_b, \sigma_8, h_0, n_s, w_0) = (0.2664, 0.0492, 0.831, 0.6727, 0.9645, -1.0)$. We note that in the 6-parameter inference there are visible projection effects on Ω_c in most models, induced by the degeneracy between Ω_c and w_0 (in the bottom-left panel of Fig. 4). Since w_0 is only marginally constrained and has an asymmetric prior, it shifts the mean of the posterior for correlated parameters. As Ω_c and σ_8 are highly correlated as well, this also induces a bias on σ_8 . Curiously, both PersLay statistics seem to be most robust against that. This behavior is consistent across multiple random seeds.

J Architectures and training hyperparameters

This appendix describes the architectures, simulation data, compression schemes, and training hyperparameters used in the reported experiments. The notation here follows the paper, while Table 9 also gives the corresponding configuration names used in the released code. The lensing configuration files are generated over one two-parameter cosmological pair, the $0m_s8$ pair, five tomographic bins, and five independent data seeds; the main weak-lensing tables report unless stated otherwise.

J.1 Common pipeline structure and code mapping

Every method is implemented as the composition of Eq. (2). For topological methods, the filtration f_ϕ produces a scalar field or filtration values, persistent homology is computed in dimensions H_0 and H_1 , and the vectorization V_ϕ maps the resulting persistence diagrams to Euclidean features. For non-topological baselines, the persistence and diagram-vectorization stages are replaced by the identity.

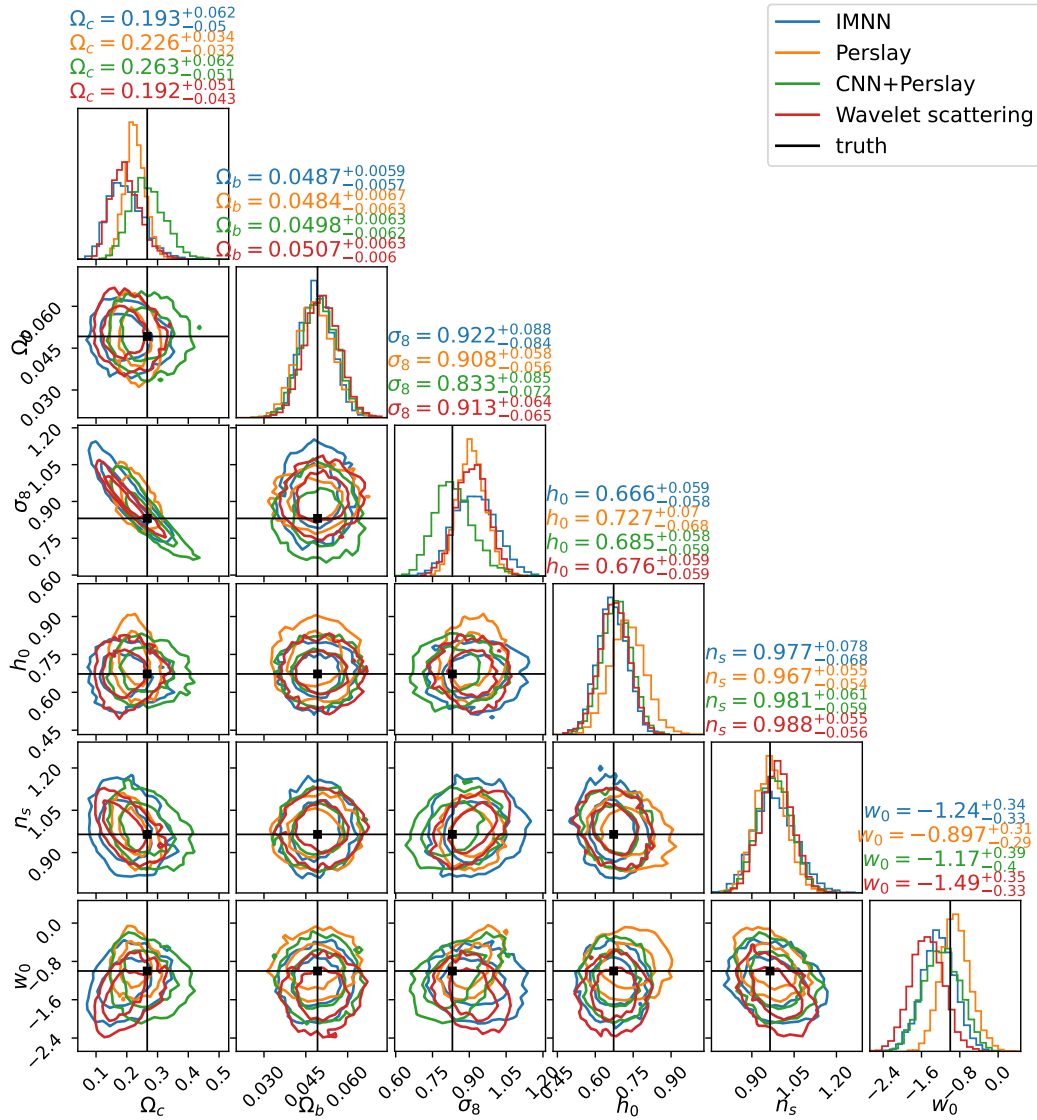


Figure 4: Comparison of SBI constraints from different summary statistics over an extended set of cosmological parameters. The contours show the 1- and 2- σ uncertainties of the different models. The equation of state of dark energy w_0 is particularly interesting to cosmologists.

Table 9: Mapping of all the methods used in the analysis. “Trainable stage” refers to parameters updated by the TopoFisher loss. MOPED is fitted from simulation summaries and carries no optimizer-updated parameters.

Method	Filtration / summary	Vectorization	Trainable stage
$\log(C_\ell)$	power spectrum	identity	none
Peak counts	peak-count histogram	identity	none
Wavelet scattering	WST coefficients	identity	none
Cubical-PI	fixed cubical PH	persistence image	none
Cubical-Silhouette	fixed cubical PH	persistence silhouette	none
Cubical-Curves	fixed cubical PH	differentiable curves	none
TF-Cubical-PersLay	fixed cubical PH	PersLay	vectorization
TF-CNN-PersLay	learned CNN filtration + PH	PersLay	filtration and vectorization
IMNN	strided CNN encoder + dense summary head	identity	CNN encoder and dense head

J.2 Filtrations and fixed scientific summaries

Fixed cubical persistence. The fixed topological pipelines use a periodic cubical filtration of the input field and compute persistence diagrams in homology dimensions H_0 and H_1 . In the code this is the cubical filtration with `homology_dimensions: [0,1]`, `periodic: true`, and a GUDHI backend. The same filtration is used by Cubical-PI, Cubical-Silhouette, Cubical-Curves, and TF-Cubical-PersLay. For the large lensing runs, persistence features for some fixed-vectorization baselines are cached on disk when useful for throughput.

Power spectrum baseline. The $\log(C_\ell)$ baseline computes the radially averaged auto-power spectrum of each tomographic convergence map. We use 30 logarithmically spaced multipole bins, exclude the DC mode with $k_{\min} = 1$, set the field size to 512, and apply a logarithmic transform to the binned power spectrum before MOPED compression. This baseline is deterministic and has no trainable parameters.

Peak-count baseline. Peak counts are computed by identifying pixels that are strictly greater than their eight nearest neighbours. We discard a one-pixel boundary, bin peak heights into 20 uniformly spaced bins over $\kappa \in [-0.05, 0.20]$, and apply the transform $n_i \mapsto \log(1 + n_i)$ to Gaussianize the count vector before MOPED compression.

Wavelet scattering baseline. The wavelet scattering transform (WST) baseline uses the second-order scattering transform [Villar-Corrales and Morgenshtern, 2021] as implemented in KYMATIO [Andreux et al., 2020]. For each 512×512 map we use $J = 5$ dyadic scales, $L = 4$ orientations, and maximum scattering order 2. The feature vector contains the spatial mean S_0 , 20 first-order coefficients S_1 , and 160 second-order coefficients S_2 , for a total of 181 features. We apply $\log(1 + \cdot)$ to the non-negative S_1 and S_2 coefficients and leave S_0 unchanged.

Learnable CNN filtration for TF-CNN-PersLay. The TF-CNN-PersLay pipeline prepends a full-resolution CNN before cubical persistence: a two-layer CNN with 8 hidden channels, 3×3 kernels, circular padding, and initialization scale 0.1. The CNN output is standardized before persistence, and the persistence backend computes H_0 and H_1 diagrams using the T construction with sub-batches of 100 maps. The CNN and PersLay stages are both optimized by the TopoFisher loss. During the main runs, the CNN is kept frozen for the first 1000 epochs while PersLay and the MOPED statistics stabilize, and is then unfrozen for joint optimization.

IMNN baseline. The IMNN baseline is an unconstrained non-topological Fisher-neural reference following the principle of Information Maximising Neural Networks [Charnock et al., 2018]. It consists of a strided convolutional encoder followed by a dense head that directly outputs $n_{\text{summaries}} = d$ summaries, where d is the number of parameters in the local Fisher analysis. In all two-parameter experiments reported here, $d = 2$. The persistence and vectorization stages are replaced by the identity, and the compression stage is also the identity: the dense head itself is the learned compressor.

For the GRF benchmark, the encoder has channel widths [16, 32, 16], kernel sizes [5, 3, 3], strides [2, 2, 2], and circular padding. The 64×64 input is reduced to an 8×8 spatial representation and flattened before a dense head with hidden width 64 and output dimension 2.

For the weak-lensing benchmark, the encoder has channel widths [16, 32, 32, 32, 16], kernel sizes [7, 5, 3, 3, 3], strides [4, 2, 2, 2, 2], and circular padding. The 512×512 input is reduced to an 8×8 spatial representation and flattened before a dense head with hidden width 128 and output dimension 2.

J.3 Diagram vectorizations

Identity. The identity vectorization is used by non-topological summaries such as IMNN, $\log(C_\ell)$, peak counts, and WST: the output of the filtration is directly passed to the compressor.

Persistence images. Cubical-PI uses persistence images [Adams et al., 2017] with an 8×8 grid, bandwidth 1.0, and persistence weighting. We compute features separately for H_0 and H_1 and concatenate the two outputs.

Persistence silhouettes. Cubical-Silhouette uses uniformly weighted persistence silhouettes with 50 grid points per homology dimension and a 99-th percentile support clip. The H_0 and H_1 silhouette vectors are concatenated before compression.

Differentiable persistence curves. Cubical-Curves uses differentiable cumulative curves of diagram coordinates. For the lensing runs, the vectorization uses birth and death curves (curves: "B,D"), 50 grid points, a 99-th percentile support clip, minimum persistence 0, and soft-sigmoid temperature 2. For the GRF runs, where diagram values have a different scale, we use the same curve family with 50 grid points and the GRF-specific temperature reported in Table 11.

PersLay. PersLay [Carrière et al., 2020] is the learnable diagram vectorization used by TF-Cubical-PersLay and TF-CNN-PersLay. It is applied separately to the H_0 and H_1 diagrams. The main configuration uses a 16-dimensional point embedding, a hidden dimension of 32, no post-pooling MLP (post_pool_dim: 0), and spectral normalization on the linear layers.

J.4 Compression and Fisher estimation

Unless stated otherwise, all field-based GRF and lensing pipelines use MOPED compression (Appendix B) as the final linear map before Fisher estimation, with output dimension $d = 2$ matching the parameter dimension. The covariance inverse entering the MOPED operator is Hartlap-corrected as described in Appendix B. The IMNN is the only exception: its dense head outputs a two-dimensional summary directly, so the compression stage is the identity.

Periodic MOPED refitting. For fixed pipelines, MOPED is fitted once from the relevant simulator dataset and held constant. For pipelines with learnable vectorizations or filtrations, the feature distribution drifts during training, so the MOPED operator must be periodically re-estimated. In the main lensing TF-Cubical-PersLay runs, we refit MOPED every 50 optimizer epochs. In the full-resolution TF-CNN-PersLay runs, both MOPED and the PersLay input normalization are refreshed every 50 epochs using at most 1,000 samples; this cap avoids repeatedly processing the full 17,500-sample training split at 512^2 resolution. These refits update only the linear compression and normalization statistics; the optimizer-updated parameters remain those listed in Table 9.

Transfer-Fisher protocol. For transfer-Fisher evaluations on LPT maps, the learned nonlinear stages (CNNs, PersLay weights, and/or IMNN weights) are loaded from the corresponding lognormal checkpoint and kept fixed. For MOPED-based methods, the empirical covariance, finite-difference Jacobians, precision matrix, and MOPED operator are then re-estimated on the LPT evaluation dataset, exactly as in any Fisher-information measurement. For the IMNN, there is no MOPED operator to refit; we evaluate the frozen two-dimensional network output and re-estimate only the Fisher statistics on LPT maps. Transfer results therefore test whether the learned feature extractor transfers; they do not retrain or fine-tune learned filtrations, vectorizations, or neural summaries on LPT maps.

J.5 Simulation dataset and finite differences

Noisy spiral datasets. For the spiral benchmark, each point cloud contains $N = 240$ points, with target parameters $\theta = (\mu, w)$. We use the finite-difference simulator datasets described in Section 4.1: $n_s = n_d = 10,000$ samples per configuration and five independent seeds. All point-cloud pipelines operate on k -nearest-neighbour distance features with $k = 100$ for the main table.

GRF datasets. For the GRF benchmark, each sample is a zero-mean periodic 64×64 field with power spectrum $P(k) = A_s(k/k_{\text{pivot}})^{-B}$. We use $\theta_{\text{fid}} = (A_s, B) = (1, B_0)$ with $B_0 \in \{-2, -1, 0, 1, 2\}$, finite-difference steps $\Delta\theta = (0.1, 0.1)$, and $n_s = n_d = 40,000$ simulations per configuration over five seeds. The same train/validation/test split fractions as above are used.

Lensing dataset. Weak-lensing convergence maps are generated with the `sbi_lens` lognormal simulator [List et al., 2023] at 512×512 resolution over a $10^\circ \times 10^\circ$ field of view and five tomographic bins. Maps are smoothed with a Gaussian kernel of width $\sigma = 2'$ before any summary statistic is computed. For every configuration we use $n_s = 20,000$ fiducial simulations for covariance estimation and $n_d = 20,000$ simulations at each finite-difference point for derivative estimation. The training/validation/test split fractions are 0.875/0.0625/0.0625.

For the LPT transfer experiment we use a separate LPT dataset at the same resolution, smoothing scale, tomographic-bin definition, and `0m_s8` finite-difference grid. Transfer configurations contain no training block: checkpoints are supplied at runtime, learned weights are frozen, and Fisher quantities are evaluated on the LPT dataset.

J.6 Training protocol and hyperparameters

Training uses structured minibatches containing fiducial simulations for covariance estimation and paired finite-difference simulations for derivative estimation. At each optimizer step, the loss is the negative log-determinant Gaussian Fisher loss of Eq. (4), optionally augmented by skewness and excess-kurtosis penalties on the compressed summary. Validation is performed on a held-out simulator dataset, and early stopping uses the validation Fisher loss.

Unless stated otherwise, optimization uses Adam with weight decay 10^{-4} , `ReduceLROnPlateau` scheduling with multiplicative factor 0.5 and minimum learning rate 10^{-6} , validation every 10 epochs, and five independent data seeds.

Table 10: Main lensing training hyperparameters. Fixed baselines have no optimizer-updated parameters; their entries indicate the estimator and split configuration used by the common training/evaluation driver. Here λ_s and λ_k are the skewness and excess-kurtosis penalties.

Pipeline	Epochs	LR	Batch	Patience	Clip	(λ_s, λ_k)	Extra settings
Fixed MOPED baselines	2000	10^{-3}	50	100	1.0	(0.05, 0.2)	No trainable weights; MOPED fit/evaluation only.
TF-Cubical-PersLay	2000	10^{-3}	50	100	1.0	(0.05, 0.2)	MOPED refit every 50 epochs; <code>min_delta</code> = 10^{-6} .
TF-CNN-PersLay	2500	3×10^{-4}	32	200	0.5	None	LR warm-up 50; loss clamp 20; NaN recovery; CNN frozen for first 1000 epochs; MOPED and PersLay renormalization every 50 epochs, capped at 1000 samples.
IMNN	4000	5×10^{-4}	100	400	1.0	(0.10, 0.00)	Cosine LR schedule; identity compression; dense head outputs two summaries directly.

All lensing runs use train/validation/test fractions 0.875/0.0625/0.0625. The LR scheduler patience is 20 for the fixed baselines, TF-Cubical-PersLay, and IMNN, and 30 for TF-CNN-PersLay.

The GRF differentiable-curve vectorization uses birth, death, and persistence curves on 50 grid points with a 99.9-th percentile support clip and temperature 0.1. The lensing curve vectorization instead uses birth and death curves, a 99-th percentile support clip, and temperature 2, matching the larger dynamic range of 512^2 convergence maps.

Table 11: GRF training hyperparameters. These settings are shared across $B_0 \in \{-2, -1, 0, 1, 2\}$ and five seeds.

Pipeline family	Epochs	LR	Batch	Patience	(λ_s, λ_k)	Extra settings
Fixed topological baselines	2000	10^{-3}	500	100	(0.05, 0.20)	MOPED compression; no trainable filtration/vectorization.
TF-Cubical-PersLay	2000	10^{-3}	500	100	(0.05, 0.20)	MOPED refit every 50 epochs.
TF-CNN-PersLay	2000	10^{-3}	500	100	(0.05, 0.20)	LR warm-up 50; loss clamp 20; NaN recovery; MOPED refit every 50 epochs.
IMNN	4000	5×10^{-4}	200	400	(0.10, 0.00)	Cosine LR schedule; identity compression; dense head outputs two summaries directly.

Table 12: Representative wall-clock times for the reported pipelines. Lensing jobs are one tomographic bin \times one seed; GRF jobs are one B_0 value \times one seed. Times are median scheduler wall-clock times.

Benchmark	Pipeline	Resource request	Median time/job
Lensing	$\log(C_\ell)$	4 CPU, 32 GB	12 min
	Peak counts	4 CPU, 32 GB	22 min
	Cubical-Silhouette	32 CPU, 120 GB	40 min
	Cubical-Curves	32 CPU, 120 GB	40 min
	Cubical-PI	32 CPU, 120 GB	48 min
	Wavelet scattering	16 CPU, 120 GB	301 min
	TF-Cubical-PersLay	32 CPU, 384 GB	63 min
	TF-CNN-PersLay	1 A100/H100, 200 GB	190–270 min
	IMNN	1 H100, 200 GB	13 min
GRF	Cubical-PI/Silhouette/Curves	32 CPU, 120 GB	4–6 min
	TF-Cubical-PersLay	32 CPU, 128 GB	6 min
	TF-CNN-PersLay	1 A100/H100	7–8 h
	IMNN	1 A100/H100	7 min

Hardware and caching. GRF runs at 64^2 resolution are CPU-friendly. Lensing runs involving full-resolution 512^2 persistence use a single large-memory GPU for the CNN/persistence forward and backward passes, with sub-batching inside the persistence layer. Fixed-vectorization lensing baselines use cached persistence features when available. End-to-end timing and persistence-backend details are reported separately in the scalability appendix.

K Compute resources and running times

All experiments were run on an anonymized institutional HPC cluster with CPU-only nodes and single-GPU jobs. CPU nodes used AMD EPYC-class processors with 256 GB–1 TB RAM; GPU jobs used one NVIDIA A100 40 GB or one NVIDIA H100 80 GB accelerator. CPU persistence jobs used up to 32 cores per task (gudhi parallelism), while GPU jobs requested a single accelerator. Wall-clock times below are medians measured from scheduler logs. For lensing, one job means one tomographic bin and one random seed; for GRFs, one job means one spectral index B_0 and one random seed.